Geophysical Journal International

Geophys. J. Int. (2020) **220,** 278–295
Advance Access publication 2019 June 14
GJI Marine geosciences and applied geophysics

doi: 10.1093/gji/ggz278

Evolution of heat flow, hydrothermal circulation and permeability on the young southern flank of the Costa Rica Rift

Kannikha Parameswari Kolandaivelu [1], Robert N. Harris [2], Robert P. Lowell,[1] Adam H. Robinson,[3] Dean J. Wilson[3] and Richard W. Hobbs[3]

[1] *Department of Geosciences, Virginia Polytechnic Institute and State University, Blacksburg, VA* 24061, USA. *E-mail: kannikha@vt.edu*
[2] *College of Earth, Ocean, and Atmospheric Sciences, Oregon State University, Corvallis, OR* 97331, USA
[3] *Department of Earth Sciences, Durham University, Durham DH*1 *3LE, UK*

Accepted 2019 June 12. Received 2019 June 5; in original form 2018 September 16

SUMMARY

We analyse 67 new conductive heat-flow measurements on the southern flank of the Costa Rica Rift (CRR). Heat-flow measurements cover five sites ranging in oceanic crustal age between approximately 1.6 and 5.7 Ma, and are co-located with a high-resolution multichannel seismic line that extends from slightly north of the first heat-flow site (1.6 Ma) to beyond ODP Hole 504B in 6.9 Ma crust. For the five heat-flow sites, the mean observed conductive heat flow is ≈85 mW m^{-2}. This value is approximately 30 per cent of the mean lithospheric heat flux expected from a half-space conductive cooling model, indicating that hydrothermal processes account for about 70 per cent of the heat loss. The advective heat loss fraction varies from site to site and is explained by a combination of outcrop to outcrop circulation through exposed basement outcrops and discharge through faults. Supercritical convection in Layer 2A extrusives occurs between 1.6 and 3.5 Ma, and flow through a thinly sedimented basement high occurs at 4.6 Ma. Advective heat loss diminishes rapidly between ≈4.5 and ≈5.7 Ma, which contrasts with plate cooling reference models that predict a significant deficit in conductive heat flow up to ages ≈65 ± 10 Ma. At ≈5.7 Ma the CRR topography is buried under sediment with an average thickness of ≈150 m, and hydrothermal circulation in the basement becomes subcritical or perhaps marginally critical. The absence of significant advective heat loss at ≈5.7 Ma at the CRR is thus a function of both burial of basement exposure under the sediment load and a reduction in basement permeability that possibly occurs as a result of mineral precipitation and original permeability at the time of formation. Permeability is a non-monotonic function of age along the southern flank of the CRR, in general agreement with seismic velocity tomography interpretations that reflect variations in the degree of ridge-axis magma supply and tectonic extension. Hydrothermal circulation in the young oceanic crust at the southern flank of CRR is affected by the interplay and complex interconnectedness of variations in permeability, sediment thickness, topographical structure, and tectonic and magmatic activities with age.

Key words: Permeability and porosity; Heat flow; Hydrogeophysics; Hydrothermal systems.

1 INTRODUCTION

The temporal and spatial evolution of oceanic crust and lithosphere are largely controlled by thermally mediated processes. Parsons & Sclater (1977), Stein & Stein (1994), Hasterok (2013) and Qiuming (2016) have derived somewhat different plate cooling models based on global heat-flow determinations and using various functions based on oceanic crustal age. The widely used Stein & Stein (1992) model was derived from a global analysis of heat flow and bathymetry data and suggests that predicted conductive heat flow from cooling lithosphere follows the expressions

$$q_b = 510\,\tau^{-1/2} \quad \text{for } 1\text{ Ma} \le \tau \le 55\text{ Ma} \tag{1a}$$

$$q_b = 48 + 96\exp(-\tau/36) \quad \text{for } \tau > 55\text{ Ma}, \tag{1b}$$

where q_b is the heat flow in mW m^{-2} and τ is the lithospheric age in Ma.

Measurements of conductive heat flow, particularly in young crust, typically lie well below conductive cooling curves (Baker

et al. 1991; Langseth *et al.* 1992; Fisher *et al.* 2003a; Hutnak *et al.* 2008). This discrepancy has long been attributed to heat loss by hydrothermal circulation (e.g. Elder 1965; Langseth & Von Herzen 1970; Lister 1972) and on a global scale, the difference between observed and predicted conductive heat losses indicates that hydrothermal circulation accounts for about 30 per cent of the global oceanic heat flux (e.g. Williams & Von Herzen 1974; Sclater *et al.* 1980; Elderfield & Schultz 1996; Davies & Davies 2010; Hasterok 2013). Of this, approximately 20–30 per cent occurs between 0 and 1 Ma, with the remainder occurring off axis (Stein & Stein 1994; Elderfield & Schultz 1996). Fig. 1(a) shows the predicted cooling curve from eqs (1a) and (1b) along with globally observed values with their standard deviation averaged in 2 Ma bins.

The style of hydrothermal circulation and heat transfer changes as the crust and lithosphere age from 'active' high-temperature magma-driven hydrothermal circulation at ages < 0.1 Ma (Macdonald 1982) to 'passive' lower temperature circulation on the ridge flanks (Lister 1982). The style of the ridge flank hydrothermal circulation also evolves with lithospheric age. The passive circulation may initially extend to a depth of 6 km into the young crust (Cherkaoui *et al.* 2003; Craft & Lowell 2009; Theissen-Krah *et al.* 2011; Hasenclever *et al.* 2014), and this deep crustal cooling may affect thermal regime of the ridge flank to an age of ∼5 Ma (Spinelli & Harris 2011). As the lithosphere ages the circulation tends to be restricted to the extrusive layer (Fisher 1998; Becker & Davis 2004), which typically consists of a highly permeable layer ≈ 150 m thick overlying a less permeable extrusive layer ≈ 400 m thick (Becker 1985; Salisbury *et al.* 1985). The extrusive layer, commonly referred to as crustal Layer 2A, will be designated as 2A*u* and 2A*l* to represent the upper and lower extrusive layers, respectively. As sediment thickness increases, recharge and discharge becomes restricted to exposed basement and faults (Wheat *et al.* 2004; Hutnak *et al.* 2006, 2008; Fisher & Harris 2010; Anderson *et al.* 2012).

As the thickness of low permeability sediments increases and oceanic basement topography becomes fully covered, fluid discharge to the ocean declines. Moreover, mineral precipitation and alteration may reduce crustal permeability, and reduced buoyancy forces may also impact the vigour of hydrothermal circulation (e.g. Jarrard *et al.* 2003). The conductive heat flow gradually approaches the predicted lithospheric cooling curve due to these processes that decrease the driving forces and increase the impeding forces for hydrothermal circulation.

When the conductive heat flow and the cooling curve coincide, the crust is termed 'sealed' (e.g. Anderson & Hobart 1976; Stein & Stein 1994), implying that hydrothermal circulation no longer affects the surface heat flow significantly. A statistical analysis of the global heat-flow data set indicates that on average the sealing age corresponds to a basement age of 65 ± 10 Ma (Fig. 1a; Stein & Stein 1994). This condition does not mean that hydrothermal circulation is absent. Rather it indicates that if hydrothermal circulation is present it is simply redistributing heat within the crust and does not transfer heat by advection from the crust to the ocean. Studies show that significant advective fluid flow can occur at basement ages much older than the global average 'sealing age' (e.g. Embley *et al.* 1983; Von Herzen 2004; Fisher & Von Herzen 2005).

The dominant mechanism leading to the cessation of advective heat loss through the seafloor is debated. Based on their analysis of the global data set, Stein & Stein (1994) argue that hydrothermal flow decreases as a result of decreased layer 2 porosity and permeability rather than from burial by sediment. This argument runs counter to results from heavily sedimented ridges. Detailed heat-flow studies on the thickly sedimented eastern flank of the Juan de Fuca Ridge (JDFR; Davis *et al.* 1997, 1999; Fisher *et al.* 2003b; Spinelli & Fisher 2004) show that mean observed heat flow reaches the predicted curve at ∼1.5 Ma. In addition, heat-flow studies at the Costa Rica Rift (CRR) flank showed that the mean heat flow was near the predicted cooling curve near ODP Hole 504B for which the crustal age was initially estimated to be 5.9 Ma (Langseth *et al.* 1983, 1988, Davis *et al.* 2004; Hobart *et al.* 1985). Revised estimates based on magnetic data suggest that the crustal age at Hole 504B is ≈6.9 Ma (Wilson & Hey 1995; Worm *et al.* 1996; Wilson *et al.* 2003) which we adopt in this paper. Although ≈6.9 Ma is older than the previously estimated ≈5.9 Ma for Hole 504B, the conductive cooling curve is relatively flat over this 1 Ma age difference. The studies on heavily sedimented ridges suggest that the accumulation of relatively impermeable and laterally continuous sediment is the likely cause of a sealed system at these locations. Further, global compilations of permeability measurements and seismic velocity indicate that the greatest change in the physical properties of the basement occurs in the first 10 Ma (Fisher & Becker 2000), leaving the role of crustal permeability in the sealing age an open question.

Heat-flow studies on the flanks of young heavily sedimented oceanic crust such as JDFR and CRR provide opportunities to better understand the evolution of hydrothermal circulation and mechanisms of advective heat transport within a limited age and distance from the spreading centre. In addition, such studies provide insight into crustal alteration (e.g. Alt 1995), seismic velocity structure (e.g. Carlson 2011, 2014) and microbial processes (e.g. Huber *et al.* 2003) that are linked to the thermal regime of the crust.

In this paper, we analyse 67 new conductive heat-flow measurements from the southern flank of the CRR at sites ranging in age between ∼1.6 and ∼5.7 Ma. In our analysis, we also include previously collected heat-flow data (Anderson & Hobart 1976; Langseth *et al.* 1983, 1988; Hobart *et al.* 1985; Davis *et al.* 2003, 2004). The new sites are labelled PB02 to PB06 (Fig. 2) and are co-located along a seismic reflection and multibeam bathymetry profiles, which enable an integrated analysis that elucidates the influence of basement topography and sediment thickness on fluid flow, advective heat transport and changes in the hydrothermal regime as the crust evolves with age.

2 GEOLOGIC SETTING

The Panama Basin, located in the equatorial Pacific, is bounded by the Cocos Ridge to the north and west, Carnegie Ridge to the south, and Ecuador Trench and Americas to the east. Three spreading centres are located in the basin: CRR, Ecuador Rift (ER), and the Galapagos Rift (GR; Lonsdale & Kiltgord 1978; Fig. 2). The southern flank of the CRR, the focus of our study, has an average half-spreading rate of approximately 3.3 cm yr^{-1} based on the distance from the CRR axis to the Hole 504B of age 6.9 Ma (Wilson & Hey 1995; Worm *et al.* 1996; Wilson *et al.* 2003). The green box (Fig. 2) shows the region where complementary geophysical measurements were made. The seismic reflection profile, the locations of heat-flow and other geophysical data, including swath bathymetry are shown in Fig. 2.

3 DATA

3.1 Seismic reflection measurements

A 270 km high-resolution seismic reflection profile (RS-A), along which heat-flow measurements were co-located, was collected with

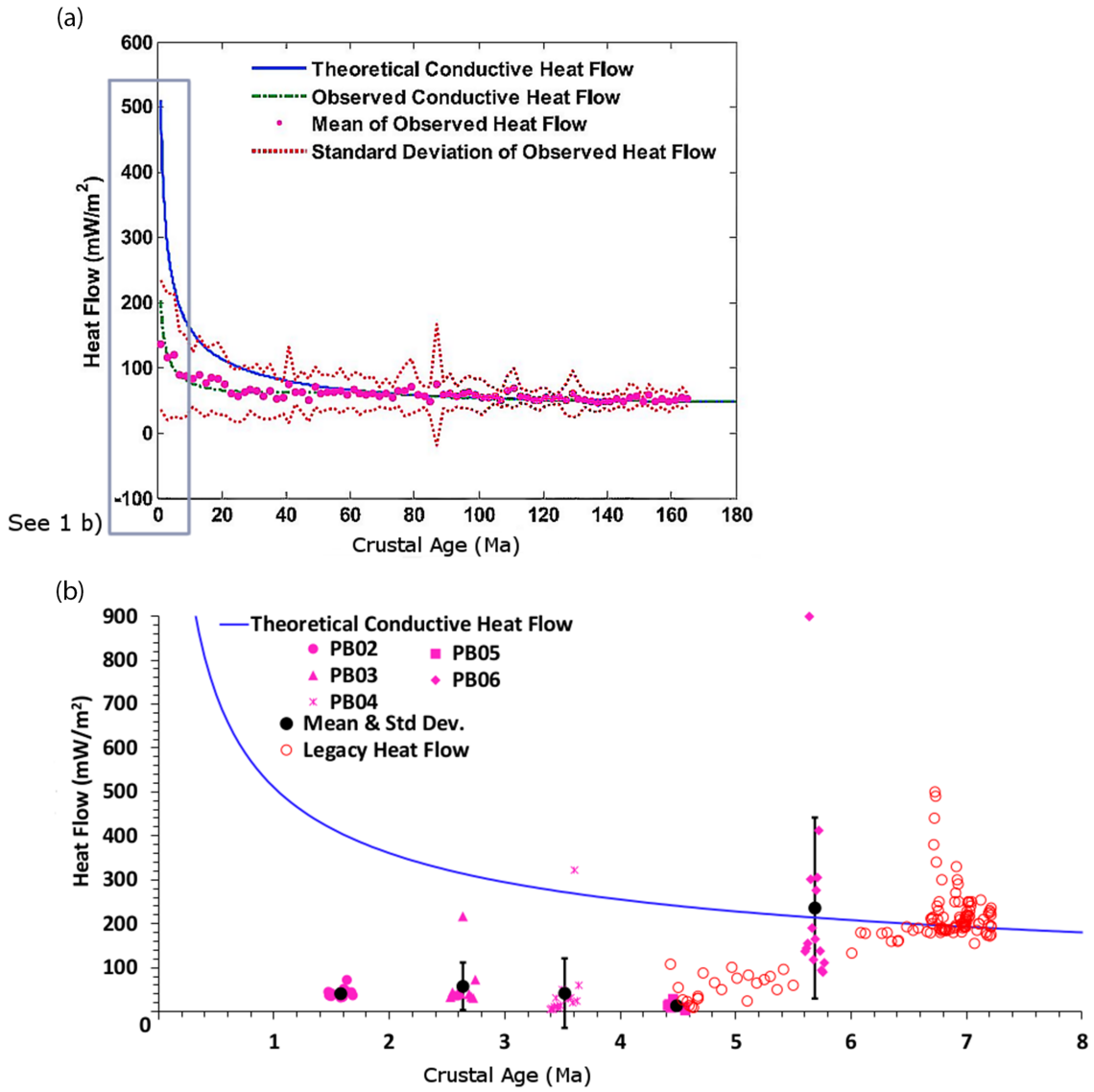

Figure 1. (a) Conductive heat loss as a function of oceanic crustal age. The blue line shows predicted fit using eq. (1a). The pink dots are observed data averaged in 2 Ma bins; the red dotted lines show standard deviation; the green dotted-dashed lines show fit to the binned data (from Heberling *et al.* 2010). (b) Heat flow on the south flank of the Costa Rica Rift as a function of oceanic crustal age. The blue line shows predicted fit/conductive cooling curve from eq. (1a). Solid pink symbols are 67 new heat-flow measurements divided into five sites (PB02 at 1.6 Ma; PB03 at 2.6 Ma; PB04 at 3.5 Ma; PB05 at 4.5 Ma and PB06 at 5.7 Ma) in this study along with their mean and standard deviation in black. The red open circles show legacy heat-flow data (Anderson & Hobart 1976; Langseth *et al.* 1983, 1988; Hobart *et al.* 1985; Davis *et al.* 2003, 2004). Note that the legacy heat-flow values are projected laterally up to 10 km onto the profile in Fig. 1(b).

a GI airgun array with a source frequency ranging between 20 and 200 Hz recorded on a 4500 m multichannel hydrophone streamer with a 12.5 m group length. The resulting imaging of the sediment and the upper oceanic crust provides a geologic framework for interpreting the heat-flow data. The complete seismic section (Fig. 3) shows that sediment thickness varies considerably with thin sediment accumulations at basement highs and with thicker sediment accumulations at basement lows; the mean sediment thickness increasing from approximately 40 m at 1.6 Ma crust to 275 m at Hole 504B. The seismic profile also shows exposed basement, through going faults, and rough basement topography; however, for crust older than 5.7 Ma ($\approx$ 190 km in Fig. 3), the basement topography is more subdued and becomes completely covered with sediment.

3.2 Heat-flow data

Conductive heat-flow measurements were acquired in sediments between 50 and 250 m thick by means of a 'violin-bow' type multipenetration heat-flow probe (Hyndman *et al.* 1979). It consists of a 3.5 m sensor tube that houses 11 thermistors and a heater wire that is offset from a lance. The configuration allows the probe to be gravity-driven into the sediments and provides the sensitivity to make precise and accurate heat-flow measurements while also being robust so that many measurements can be made by 'pogo-ing' the probe along the bottom. A weight stand containing the data logger and telemetry system sits above the thermistor tube. In addition to logging the temperature time-series, the data logger also records tilt, pressure, time and the bottom water temperature. An

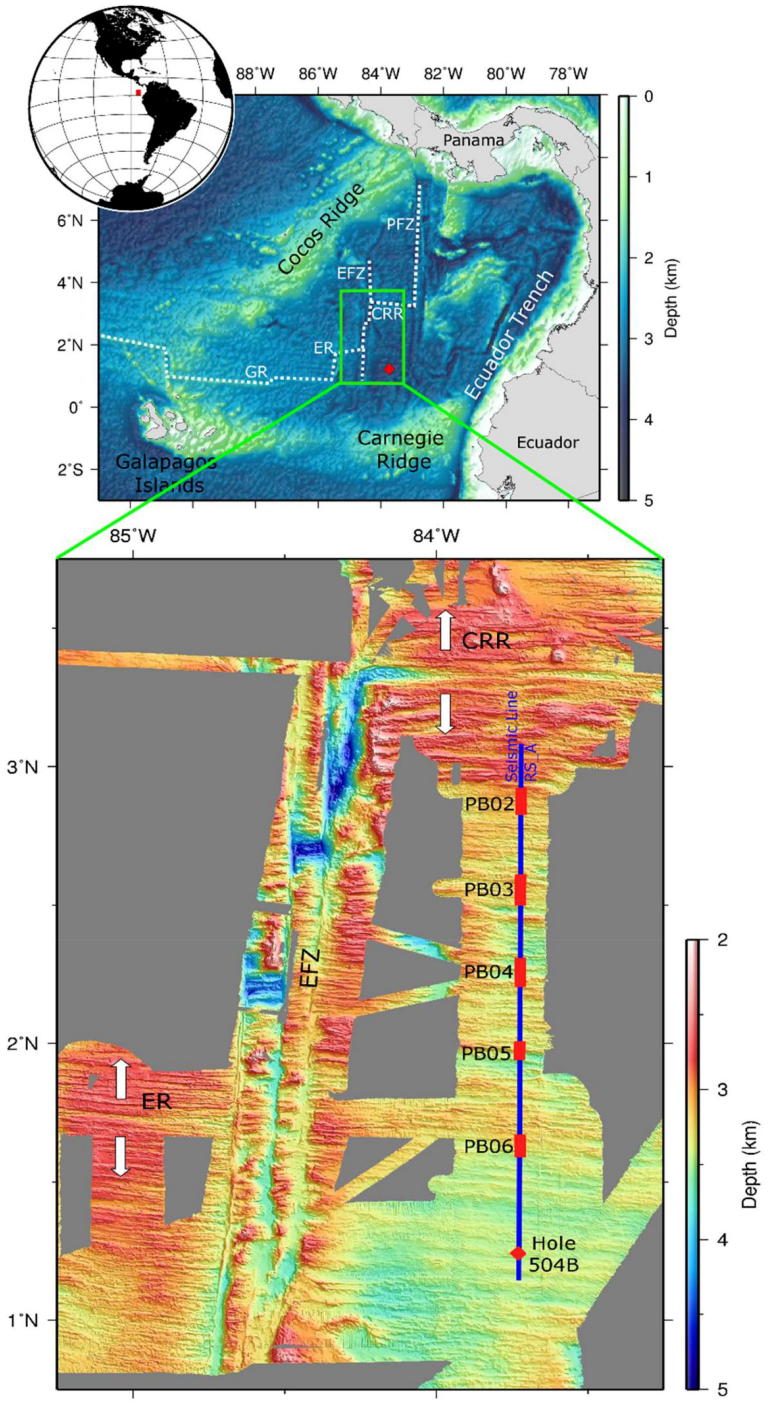

Figure 2. Location and bathymetry of the Panama Basin. The top panel gives the regional context for the Panama Basin. The basin is bounded by the Cocos Ridge to the N and W, the Carnegie Ridge to the S, and the Ecuador Trench and Americas to the E. Dashed white lines show the spreading axis (CRR = Costa Rica Rift; ER = Ecuador Rift; GR = Galapagos Rift). Transforms bounding the CRR, EFZ (Ecuador Fracture Zone) and PFZ (Panama Fracture Zone) are labelled. The red diamond shows the location of the ODP Hole 504B. The green box encloses the area where geophysical measurements were made during cruises JC112, JC113 and Sonne 0238. The bottom panel shows a zoom-in of the green box with the spreading direction of the rifts shown in white arrows. RS_A seismic profile spanning from slightly north of the first heat-flow site, PB02, to beyond ODP Hole 504B is shown in the blue line. Stations PB02 to PB05 on RS_A are shown as red solid rectangles.

ultrashort baseline sensor attached 50 m above the probe provides precise navigation. The probe allows *in situ* measurements of the shallow thermal gradients and thermal conductivity in sediments on the seafloor. The analysis of heat-flow measurements is based on the scheme presented by Villinger & Davis (1987) as implemented using SlugHeat (Stein & Fisher 2001). The *in situ* thermal gradient is based on a temperature time-series collected for 7 min, which is long enough to achieve partial equilibrium with the sediments. Equilibrium temperatures are then estimated through an extrapolation based on a line source model of radial heat conduction (Villinger

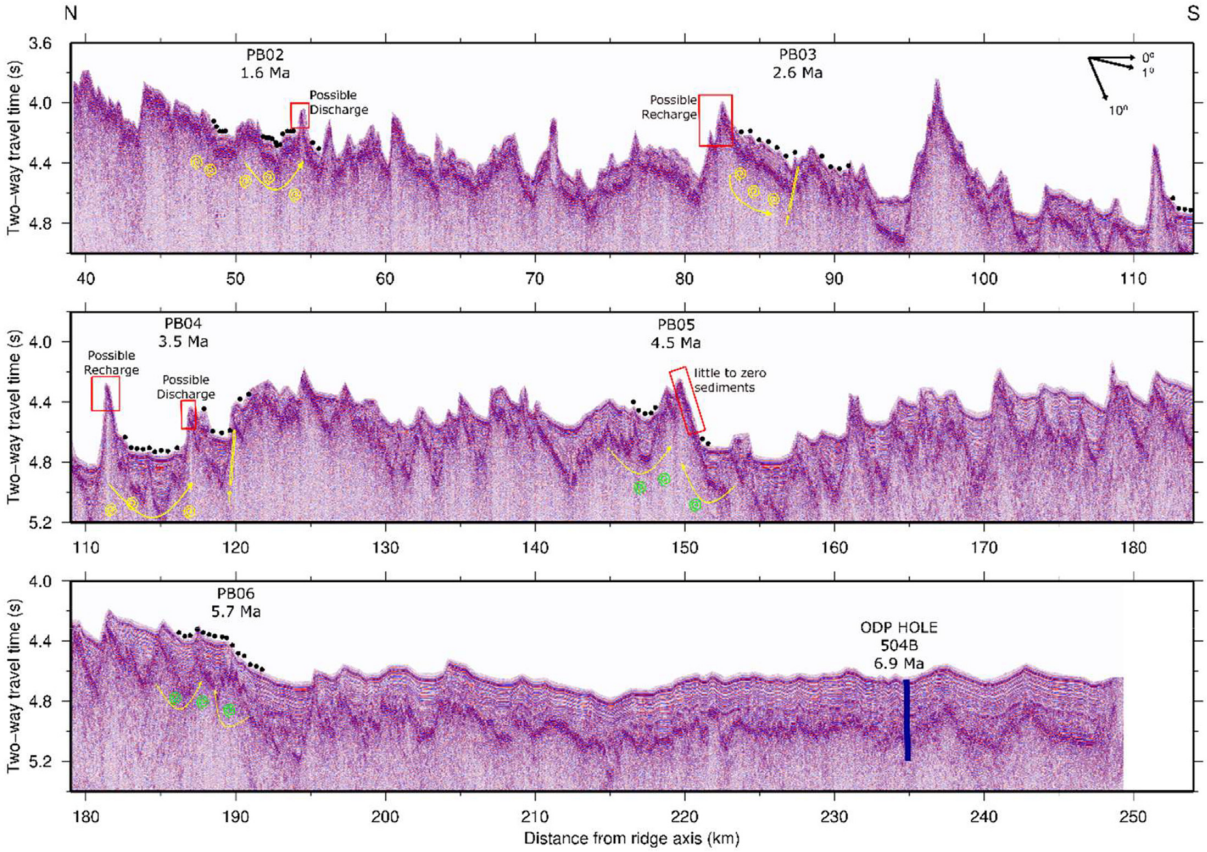

Figure 3. Pre-stack time-migrated seismic image (RS_A seismic profile) showing heat-flow stations PB02 through PB06 and ODP Hole 504B as a function of the distance from the Costa Rica Rift. Heat-flow stations PB02 through PB06 and their various heat transport mechanisms are shown. The curved yellow arrows indicate outcrop to outcrop type circulations except at PB06 where they indicate heat flow focused around buried basement highs. The yellow spirals indicate supercritical convection cells that homogenize basement temperatures. The green spirals in PB05 and PB06 indicate sub- to slightly supercritical convection which redistributes heat. The yellow parallel lines and arrows (PB03 and PB04) indicate upflow of fluids through a fault. N, North; S, South.

& Davis 1987). A calibrated heat pulse is then applied through the heater wire for 10 s and a 7 min temperature decay provides data for determining thermal conductivity. The heat flow, thermal conductivities, thermal gradient values and sediment thicknesses for all sites are given in Table 1. Heat-flow measurements were closely spaced to avoid aliasing the hydrothermal circulation signal and co-located with the swath bathymetry and seismic reflection data to better understand the measuring environment (e.g. Fisher & Harris 2010).

4 ANALYSIS

Fig. 1(b) shows the 67 new measured heat-flow values along with the previously published data (Anderson & Hobart 1976; Langseth *et al.* 1983, 1988; Hobart *et al.* 1985; Davis *et al.* 2003, 2004) and predicted heat flow based on half-space cooling curve from eq. (1a). Fig. 1(b) shows heat flow transitioning from values of about 40 mW m^{-2} at 1.6 Ma to a mean value of 235 mW m^{-2} at 5.7 Ma, which lies near the predicted cooling curve. Previously published heat-flow data indicated by the open circles in Fig. 1(b) also show that heat transfer transitions from advectively to conductively dominated values between $\approx$ 4.5 and $\approx$ 6.0 Ma.

The average measured heat flow of the 67 new measurements (Table 1) is $\sim$85 mW m^{-2}. This value is considerably less than the average expected basal heat flow of $\sim$280 mW m^{-2}, obtained by integrating eq. (1a) between 1.6 and 5.7 Ma. The heat-flow fraction (q_{obs}/q_b) is $\sim$0.3 indicating that $\sim$70 per cent ($\sim$200 mW m^{-2}) of q_b is advected. The effect of thermal rebound from deep axial cooling on the south flanks of the CRR between 1.6 and 5.7 Ma crust is small based on observational constraints and modelling studies (Fisher 2003; Spinelli & Harris 2011). Hence these effects on the overall advective heat loss fraction are negligible.

In order to quantify the mechanisms responsible for this advective heat loss, we construct a 1-D thermal conduction model of the sediment and basement as a function of age between 1.6 and 6.9 Ma at Hole 504B. This model allows us to compare the expected temperature at the sediment–basement interface (SBI) with the SBI temperature derived from the observed heat-flow measurements. The mathematical formulation is given in Appendix A. The results given by eq. (A2) show that the conduction-derived SBI temperature, expressed as the difference ΔT_{SBI} between seafloor and the base of the sediment, can be written as

$$\Delta T_{SBI}(h_s) = \frac{q_b h_s}{\lambda_s} = \frac{510\tau^{1/2} v_s}{\lambda_s}, \quad (2)$$

where 510 $\tau^{-1/2}$ is heat flow in mW m^{-2}, h_s is the sediment thickness, λ_s is the thermal conductivity of the sediment and v_s is the sedimentation rate. Over much of the heat-flow profile, the sedimentation rate is $\approx$ 25 m Ma^{-1} whereas at PB04 and PB06 it is $\approx$ 40 m Ma^{-1}, similar to that at Hole 504B (Becker *et al.* 1983). Definitions and values of symbols are given in Table 2. We use λ_s = 0.92 W

Table 1. Conductive heat-flow data from southern ridge flank of the Costa Rica Rift.

Datum	Latitude (°N)	Longitude (°W)	Sediment thickness (m)	Thermal gradient (°C km^{-1})	Thermal conductivity (W m^{-1} K^{-1})	Heat flow (mW m^{-2})	Sediment–basement interface temperature (°C)
PB02 Age = 1.6 Ma							
PB02–01	2.8897	−83.6991	41	62	0.7	45	2.0
PB02–02	2.8878	−83.6992	40	51	0.7	37	1.6
PB02–03	2.8861	−83.6993	49	52	0.7	37	2.0
PB02–04	2.8843	−83.6993	50	55	0.7	40	2.2
PB02–05	2.8825	−83.6993	50	59	0.7	42	2.3
PB02–06	2.8825	−83.6994	50	48	0.7	35	1.9
PB02–07	2.8596	−83.6998	45	48	0.7	35	1.7
PB02–08	2.8578	−83.6999	49	45	0.7	32	1.7
PB02–09	2.8560	−83.6999	51	45	0.7	33	1.8
PB02–10	2.8542	−83.6999	49	46	0.7	33	1.8
PB02–11	2.8524	−83.7000	49	47	0.7	34	1.8
PB02–12	2.8515	−83.7001	42	48	0.7	35	1.6
PB02–13	2.8497	−83.7001	27	73	0.7	52	1.5
PB02–14	2.8479	−83.7002	36	62	0.7	45	1.8
PB02–15	2.8452	−83.7003	44	60	0.7	44	2.1
PB02–16	2.8433	−83.7003	31	65	0.7	47	1.6
PB02–17	2.8416	−83.7004	21	97	0.7	72	1.6
PB02–18	2.8299	−83.7008	30	61	0.7	44	1.5
PB02–19	2.8263	−83.7008	42	52	0.7	37	1.7
		Mean	42			41	1.8
PB03 Age = 2.6 Ma							
PB03–01	2.5711	−83.7074	57	46	0.7	33	2.0
PB03–02	2.5657	−83.7075	66	61	0.7	44	3.1
PB03–03	2.5604	−83.7076	72	53	0.7	37	2.9
PB03–04	2.5549	−83.7078	86	53	0.7	38	3.6
PB03–05	2.5495	−83.7079	104	65	0.7	46	5.2
PB03–06	2.5440	−83.7080	87	58	0.7	41	3.9
PB03–07	2.5386	−83.7083	32	278	0.8	217	7.5
PB03–08	2.5224	−83.7087	46	55	0.7	40	2.0
PB03–09	2.5171	−83.7089	66	48	0.7	34	2.4
PB03–10	2.5117	−83.7090	108	44	0.7	31	3.6
PB03–11	2.5064	−83.7091	47	103	0.7	73	3.7
		Mean	70			58	3.6
PB04 Age = 3.5 Ma							
PB04–01	2.3105	−83.7124	93	9	0.7	5	0.5
PB04–02	2.3069	−83.7125	135	9	0.7	7	1.0
PB04–03	2.3033	−83.7126	159	8	0.8	5	0.9
PB04–04	2.2997	−83.7126	202	11	0.7	11	2.4
PB04–05	2.2960	−83.7126	34	44	0.7	31	1.2
PB04–06	2.2925	−83.7127	218	18	0.7	12	2.8
PB04–07	2.2888	−83.7127	318	12	0.7	8	2.8
PB04–08	2.2846	−83.7127	194	19	0.7	14	3.0
PB04–09	2.2792	−83.7126	113	71	0.7	50	6.1
PB04–10	2.2630	−83.7125	53	43	0.7	30	1.7
PB04–11	2.2576	−83.7124	110	44	0.7	31	3.7
PB04–12	2.2522	−83.7126	225	29	0.7	20	4.9
PB04–13	2.2471	−83.7126	45	437	0.7	322	15.7
PB04–14	2.2413	−83.7126	123	34	0.7	24	3.2
PB04–15	2.2359	−83.7126	33	83	0.7	60	2.1
		Mean	137			42	3.5
PB05 Age = 4.5 Ma							
PB05–01	2.0038	−83.7187	110	19	0.7	14	1.7
PB05–02	2.0003	−83.7188	126	23	0.7	17	2.3
PB05–03	1.9966	−83.7189	184	12	0.7	9	1.8
PB05–04	1.9931	−83.7191	163	17	0.7	12	2.1
PB05–05	1.9903	−83.7186	62	42	0.7	29	1.9
PB05–06	1.9620	−83.7194	45	14	0.7	10	0.5
PB05–07	1.9585	−83.7197	146	5	2.0	3	0.5
		Mean	119			13	1.5
PB06 Age = 5.7 Ma							
PB06–01	1.6453	−83.7409	140	188	0.7	137	20.8

Table 1. Continued

Datum	Latitude (°N)	Longitude (°W)	Sediment thickness (m)	Thermal gradient (°C km^{-1})	Thermal conductivity (W m^{-1} K^{-1})	Heat flow (mW m^{-2})	Sediment–basement interface temperature (°C)
PB06–02	1.6419	−83.7405	176	198	0.7	144	27.5
PB06–03	1.6388	−83.7404	135	210	0.7	155	22.8
PB06–04	1.6345	−83.7397	19	1157	0.8	899	18.8
PB06–05	1.6309	−83.7393	48	397	0.8	301	15.7
PB06–06	1.6273	−83.7391	146	259	0.7	190	30.2
PB06–07	1.6239	−83.7388	226	161	0.7	118	29.0
PB06–08	1.6193	−83.7388	168	229	0.7	165	30.1
PB06–09	1.6167	−83.7387	136	382	0.7	276	40.8
PB06–10	1.6131	−83.7381	82	418	0.7	305	27.3
PB06–11	1.6095	−83.7377	89	570	0.7	412	39.8
PB06–12	1.6060	−83.7373	104	190	0.7	138	15.6
PB06–13	1.6024	−83.7368	203	130	0.7	94	20.8
PB06–14	1.5987	−83.7365	261	125	0.7	90	25.5
PB06–15	1.5951	−83.7361	235	156	0.7	111	28.4
		Mean	145			236	26.2
				Average	0.7	≈85	≈7

Table 2. Parameters and values.

Symbol	Definition	Value	Units
$a*$	Thermal diffusivity of fluid		m^2 s^{-1}
c_f	Specific heat of water	4200	J kg^{-1} K^{-1}
g	Acceleration due to gravity	9.81	m s^{-2}
h_b	Basement thickness		m
h_s	Sediment thickness		m
k	Crustal permeability		m^2
k_{th}	Threshold crustal permeability		m^2
L	Horizontal fluid flow path length		m
q_{adv}	Advective heat flow		mW m^{-2}
q_b	Basal heat flux		mW m^{-2}
q_d	Heat flow at the discharge		mW m^{-2}
q_{obs}	Observed/measured heat flow		mW m^{-2}
Ra	Rayleigh number		
Ra_c	Critical Rayleigh number		
T_b	Basement temperature		°C
T_d	Discharge temperature		°C
T_s	Temperature of the sediment layer		°C
T_{SBI}	Predicted temperature at the sediment–basement interface		°C
T_{SBI}^{obs}	Observed temperature at the sediment–basement interface		°C
T_{sp}	Spring temperature; temperature of the upwelling fluids from a fault		°C
T_{sw}	Seawater temperature	0	°C
u	Darcian velocity of fluid		m yr^{-1}
u_z	Vertical velocity of fluids		m yr^{-1}
v_s	Sedimentation rate		m Ma^{-1}
α	Thermal expansion coefficient of water	10^{-4}	°C^{-1}
λ_b	Thermal conductivity of the basement	2	W m^{-1} K^{-1}
λ_s	Average thermal conductivity of the sediments	0.92	W m^{-1} K^{-1}
ν	Kinematic viscosity of the fluid	10^{-6}	m^2 s^{-1}
ρ_f	Density of water	1000	kg m^{-3}
τ	Age of oceanic crust		Ma

m^{-1} K^{-1}, which is the average thermal conductivity based on Hole 504B's physical property measurements (Davis *et al.* 2004). Fig. 4 shows the expected SBI temperature versus age for the two sedimentation rates, along with the average SBI temperature for the five heat-flow sites and the data at Hole 504B. The observed SBI temperature at each heat-flow point is determined from the relationship $\Delta T_{SBI}^{obs} = \frac{q_{obs} h_s}{\lambda_s}$. The average SBI temperature at each site, except PB06 and Hole 504B, is much less than predicted by conduction regardless of the sedimentation rate (Fig. 4).

In the extrusive layer of the young oceanic crust south of the CRR, supercritical thermal convection will tend to homogenize the temperature distribution within the basement rocks. The condition

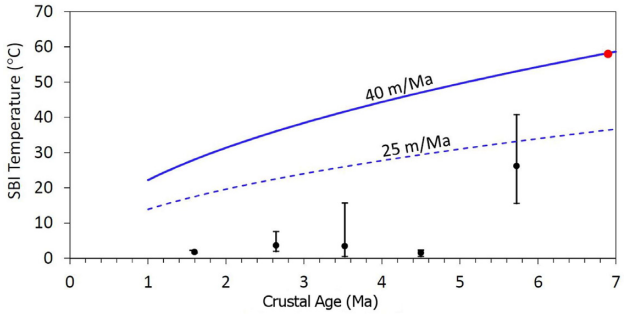

Figure 4. Sediment–basement interface (SBI) temperature as a function of crustal age. The predicted SBI temperatures for sedimentation rates of 40 m Ma^{-1} (PB04 at 3.5 Ma and PB06 at 5.7 Ma) and 25 m Ma^{-1} (PB02 at 1.6 Ma, PB03 at 2.6 Ma and PB05 at 4.5 Ma) as obtained from eq. (2) are shown as the solid blue and dotted blue lines, respectively. The black circles show the average SBI temperature (Table 1) based on the observed heat-flow data for all five sites and the bars indicate their maximum and minimum range values. Observed SBI temperature at 6.9 Ma crust in ODP Hole 504B and Hole 896A (Becker *et al.* 1983; 2004) is shown as the red circle.

for onset of convection is defined by the Rayleigh number Ra. For a layer of thickness h_b, with a fixed heat flux q_b at the base, and impermeable sediments above (Spinelli *et al.* 2004), the Rayleigh number and its critical value Ra_c are given by (Nield 1968)

$$Ra = \frac{\alpha g k q_b h_b^2}{\lambda_b a * \nu} \geq Ra_c = 27.1. \quad (3)$$

Assuming that other parameters are constant, eq. (3) shows that Ra decreases as $\tau^{1/2}$ as the crust ages because of the predicted decline of q_b. Using parameter values in Table 2, Fig. 5 displays the crustal permeability needed to exceed Ra_c for $h_b = 150$ m and $h_b = 550$ m as a function of age. These values of h_b are chosen based on logging data from Hole 504B that indicates the upper 100–200 m of the crust is significantly more permeable than then underlying extrusive section, which extends to approximately 550 m beneath the sediments (Becker *et al.* 1989). The curves in Fig. 5 show that supercritical convection at 1.6 Ma requires that k must exceed threshold values $k_{th} = 3 \times 10^{-12}$ and 2×10^{-13} m^2, for $h_b = 150$ and 550 m, respectively; whereas k_{th} must exceed 7×10^{-12} and 5×10^{-13} m^2 at 6.9 Ma for the same values of h_b. The permeability value for $h_b = 550$ m is an 'effective' value for combined Layers 2Au and 2Al, but since the thickness of 2Al is considerably greater than that of 2Au, it is assumed that the effective permeability is nearly the same as that of Layer 2Al.

When $Ra \gg Ra_c$ in a permeable layer with a given basal heat flux, vigorous convection tends to homogenize the temperature within the convecting interior, but because the heat flux is fixed, fluid convection will transport the same amount of heat as the conducting layer, hence the Nusselt number is unity. Heat advection within the basement interior will be transported across the SBI by conduction across a thin thermal boundary layer so that both heat flux and temperature at the SBI are continuous. Hence the high Ra supercritical convection regime would not by itself result in a reduction in conductive heat flow across the sediment layer or a decrease in SBI temperature, unless fluid advection can occur through the sediment layer or some other process such as outcrop to outcrop circulation or fluid discharge through faults also takes place. The observation in Fig. 4 that the SBI temperature is much less than predicted by conduction at sites PB02 through PB05 indicates that advective heat transfer is occurring. At PB06, however, the mean SBI temperature is only slightly less than the value predicted by conduction, suggesting that heat is not being advected between the crustal aquifer and the ocean.

In the following subsections, we present a detailed analysis of the heat-flow data as a function of age from the five heat-flow sites labelled PB02 through PB06. This analysis provides estimates of crustal permeability that can be compared with the Rayleigh criterion shown in Fig. 5. The goal is to determine whether there appear to be significant changes in crustal permeability as a function of age that affect the advective heat transfer. The values of calculated permeability are given in Table 3. In performing these analyses, we neglect the effects of heat-flow refraction, fluid flow through the sediments and the effect of sedimentation on reducing the observed heat flow (e.g. Hutchinson 1985; Hutnak & Fisher 2007).

Our estimates of mass flow rate and crustal permeability in the basement are largely based on the well-mixed aquifer model in which we assume that flow is dominantly parallel to the spreading direction. In reality fluid flow is likely 3-D (e.g. Winslow & Fisher 2015; Winslow *et al.* 2016), but 3-D modelling is beyond the limitations of the data and the scope of this paper. Two recent studies show the impact of flow perpendicular to the spreading direction (Fisher *et al.* 2008; Niera *et al.* 2016), and this caveat should be kept in mind when viewing the results. The likely presence of 3-D fluid flow in the natural system does not change the basic conclusion that fluid circulation advects a substantial amount of heat from this system. However, because the dominant fluid flow direction may not align with seismic line RS-A and our heat-flow stations, possible points of fluid recharge and discharge may be located east or west of the seismic line.

4.1 Heat-flow site PB02

Site PB02, the closest heat-flow station to the CRR, is located on ~1.6 Ma old oceanic basement where the mean sediment thickness is about 40 m. These 19 heat-flow measurements (Table 1) have a mean of 41 mW m^{-2} whereas $q_b \approx 400$ mW m^{-2}. These values yield a mean heat-flow deficit $(1 - q_{obs}/q_b)$ of ≈0.9 thereby giving an advective heat flow $q_{adv} \approx 360$ mW m^{-2}. The SBI temperatures have a mean and standard deviation of 1.8 and 0.2 °C, respectively, implying that the upper basement temperatures are homogenized.

Heat-flow values observed at PB02 can be grouped broadly into two sets, A and B (Fig. 6a). Set A shows uniformly low heat flow, whereas set B has a southward increasing trend in heat flow suggesting lateral transport of heat by fluid advection (Fig. 6a). The possible discharge could be at a sparsely sedimented basement exposure to the south. This interpretation is supported by the two heat-flow measurements just south of this basement high that show a northward increasing trend. Recharge could be anywhere in the north as Fig. 6(b) shows continuous thinly sedimented basement; alternatively, recharge could occur to the east or west of the seismic line. Because the SBI temperatures are relatively uniform we apply the well-mixed aquifer model of Langseth & Herman (1981) as outlined in Appendix B to estimate the lateral mass flow through the basement. The data in set B are well fit by an exponential as shown in Fig. 6(a) which could then be applied in eq. (B2) resulting in a volumetric flow rate per unit length ≈415 m^2 yr^{-1}. Using this flow rate in eq. (B4) enables us to estimate the quantity kh_b; for $h_b = 150$ and 550 m, we obtain permeabilities of $\sim 6 \times 10^{-10}$ and 5×10^{-11} m^2, respectively. These values are similar to those in Fig. 5 for $Ra \approx 100 Ra_c$. Hence vigorous supercritical convection would largely homogenize the basement temperature distribution,

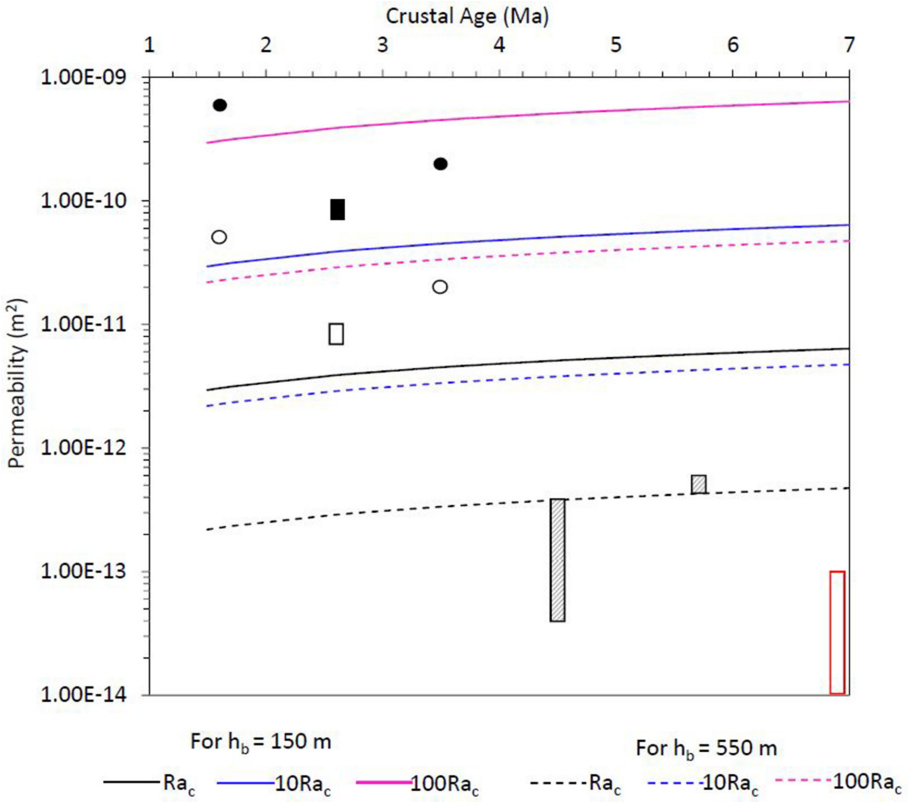

Figure 5. Estimated permeability of the crust as a function of crustal age for Ra_c, 10 Ra_c, 100 Ra_c for $h_b = 150$ m and 550 m. Solid black circles/rectangles are the estimated permeabilities/range of permeabilities at each site for $h_b = 150$ m and open black circles/rectangles are for $h_b = 550$ m. Hatched black rectangles are permeabilities where Rayleigh convection is at or near supercritical for $h_b = 550$ m. The red open rectangle indicates the permeabilities at ODP Hole 504B in 6.9 Ma crust. The permeability values calculated are given to one significant figure and have a likely uncertainty of a factor of 2 for PB02 at 1.6 Ma, PB03 at 2.6 Ma and PB04 at 3.5 Ma but larger uncertainties for PB05 at 4.5 Ma and PB06 at 5.7 Ma.

Table 3. Permeabilities of sites PB02 through PB06 and ODP Hole 504B.

Site	Age	Fractional heat flow	Advective heat flux	$\langle \Delta T_{SBI}^{obs} \rangle$	Permeability	
	(Ma)	(q_{obs}/q_b)	(mW m^{-2})	(°C)	(m^2)[a]	(m^2)[b]
PB02	1.6	0.10	360	2	6×10^{-10}	5×10^{-11}
PB03	2.6	0.18	260	4	10^{-10} to 7×10^{-11}	10^{-11} to 7×10^{-12}
PB04	3.5	0.15	230	3	2×10^{-10}	2×10^{-11}
PB05	4.5	0.06	230	2	–	4×10^{-13}
PB06	5.7	1.00	0	26	–	5×10^{-13}
Hole 504B	6.9	–	–	–	10^{-13} to 10^{-14} (Layer 2A)[c]	

[a]Assuming an aquifer thickness of 150 m.
[b]Assuming an aquifer thickness of 550 m.
[c]Anderson & Zoback (1982); Fisher *et al.* (1990); Becker (1996); Becker *et al.* (2004).

and outcrop to outcrop circulation would transport low-temperature fluid laterally and advect heat to the seafloor.

4.2 Heat-flow site PB03

This site (Fig. 7), at a crustal age of 2.6 Ma, consists of 11 measurements (Table 1). The mean sediment thickness is ≈ 70 m and mean observed heat flow is 58 mW m^{-2}. The conductive prediction, from eq. (1a), is 310 mW m^{-2} yielding a mean heat-flow deficit of about 0.82 and an advected heat flow $q_{adv} \approx 260$ mW m^{-2}.

All measurements at PB03, except one, exhibit a uniformly low heat flow. The highest heat-flow value of 217 mW m^{-2} appears to occur close to a fault (Fig. 7b) that probably serves as a discharge zone. Assuming isothermal upflow through the fault at a temperature T_{sp}, conductive heat flow is expected to decay as $1/x$, where x is the distance from the fault plane. Appendix C outlines the mathematical formulation of this problem. From eq. (C2), with $q_b = 217$ mW m^{-2} and $x = 100$ m, we calculate the temperature of the upflow, T_{sp}, in the range of 20–35 °C, depending whether we use the basalt or sediment thermal conductivity, respectively (Table 2).

The first six uniformly low heat-flow values (from ≈ 83 to 86.5 km in Fig. 7a) with the seventh being the highest at this site suggest lateral advective transport of heat by fluids with the high heat-flow point being adjacent to the discharge fault (Fig. 7b). Possible recharge could be at a sparsely sedimented basement exposure to the north (Fig. 7b). The lateral flow rates through the basement can be estimated by applying the well-mixed aquifer model of Langseth & Herman (1981) as outlined in Appendix B. From eq. (B1), the

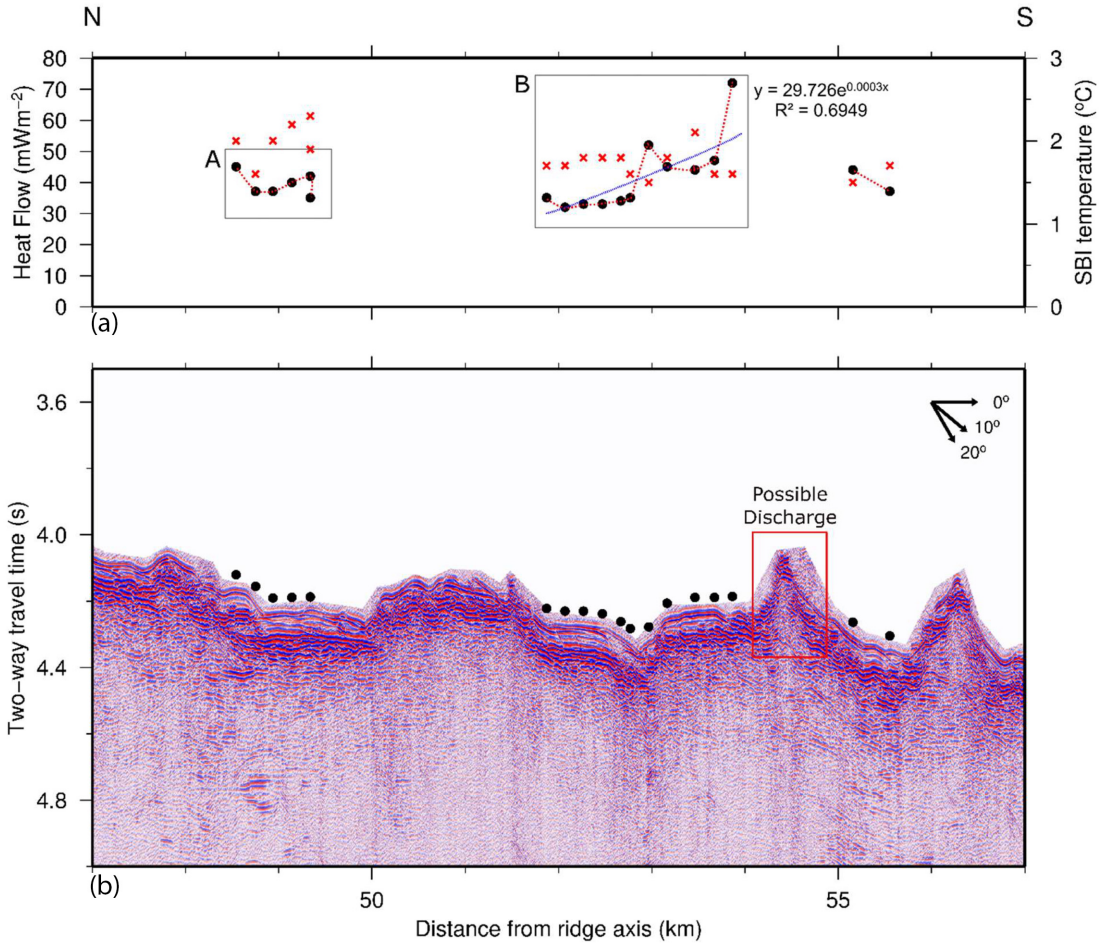

Figure 6. Site PB02 (1.6 Ma). (a) 19 heat-flow measurements (black circles) as a function of distance from the CRR axis. The red crosses show sediment–basement interface (SBI) temperatures at each heat-flow measurement. The grey boxes indicate heat-flow sets A and B discussed in the text. The blue dashed line shows best-fitting exponential function (refer eq. B2), which is the solution to eq. (B1), enabling the estimation of volumetric flow rate per unit length. R^2 shows the goodness of fit of the exponential equation. (b) Pre-stack time-migrated seismic image of PB02. The vertical axis is a two-way traveltime and the horizontal axis is the distance from the CRR in km. The red box indicates possible discharge area. N, North; S, South. Note: faults are shown only where there is circumstantial evidence of enhanced heat flow which is interpreted as that caused by focused flow along a fault.

quantity uh_b can be estimated, where $dT(x)$ is the T_{sp} calculated using the fault model. This results in uh_b of 1.6×10^{-5} m^2 s^{-1} for $T_{sp} = 20$ °C and 9.2×10^{-6} m^2 s^{-1} for $T_{sp} = 35$ °C. In eq. (B4) using $L = 5$ km (recharge outcrop to discharge fault) enables us to calculate permeabilities, k, and we obtain $k = 10^{-10}$ to 7×10^{-11} m^2 for $h_b = 150$ m and $T_{sp} = 20$–35 °C; and $k = 10^{-11}$ to 7×10^{-12} m^2 for $h_b = 550$ m and $T_{sp} = 20$–35 °C. These values fall in between $Ra \approx 10$–$100Ra_c$ (Fig. 5).

Given the low estimate of the basement temperature, these results suggest that the discharge fault transports most of the advective heat (from ≈ 83.5 to 87 km in Fig. 5) to the seafloor at this site.

4.3 Heat-flow site PB04

Site PB04 consists of 15 measurements (Table 1) located on 3.5 Ma crust. The region is covered with sediment having thicknesses ranging from 20 to 290 m. The measurements are distributed over three sediment ponds with an average heat flow of 42 mW m^{-2}. Eq. (1a) yields predicted heat flow of 272 mW m^{-2}, indicating a deficit of about 0.85, or $q_{adv} \approx 230$ mW m^{-2}.

The measurements at PB04 can be broadly grouped into two sets, C and D (Fig. 8a). Set C consists of nine measurements in a sediment pond located between two large topographic highs. Heat-flow values in set C have a mean value of 16 mW m^{-2} and display a slightly increasing trend to the south. We interpret these data to reflect outcrop to outcrop lateral heat transfer where recharge occurs at poorly sedimented basement high areas to the north of the pond and discharges through a thinly sedimented basement high to the south. The SBI temperatures have a mean and standard deviation of 2.3 and 1.7 °C, respectively, implying that the upper basement temperatures are homogenized. The data are well fit to an exponential as shown in Fig. 8(a). Hence this fit is applied to eq. (B2) in the well-mixed aquifer model (Appendix B) to estimate the volumetric flow rate per unit length ≈115 m^2 yr^{-1}. Applying this flow rate in eq. (B4), we estimate permeabilities of $\sim 2 \times 10^{-10}$ and 2×10^{-11} m^2 for $h_b = 150$ and 550 m, respectively. These values are similar to those for $Ra \approx 100Ra_c$ (Fig. 5). Thus, supercritical buoyancy-driven convection significantly homogenizes the temperature distribution within the basement.

In set D, three measurements are of uniformly low heat flow and one exhibits the highest heat flow of 322 mW m^{-2} at this site. This high heat flow appears to occur close to a fault (Fig. 8b) which could serve as a discharge zone. We can use the fault model methodology outlined in Appendix C and used in the analysis of PB03. From

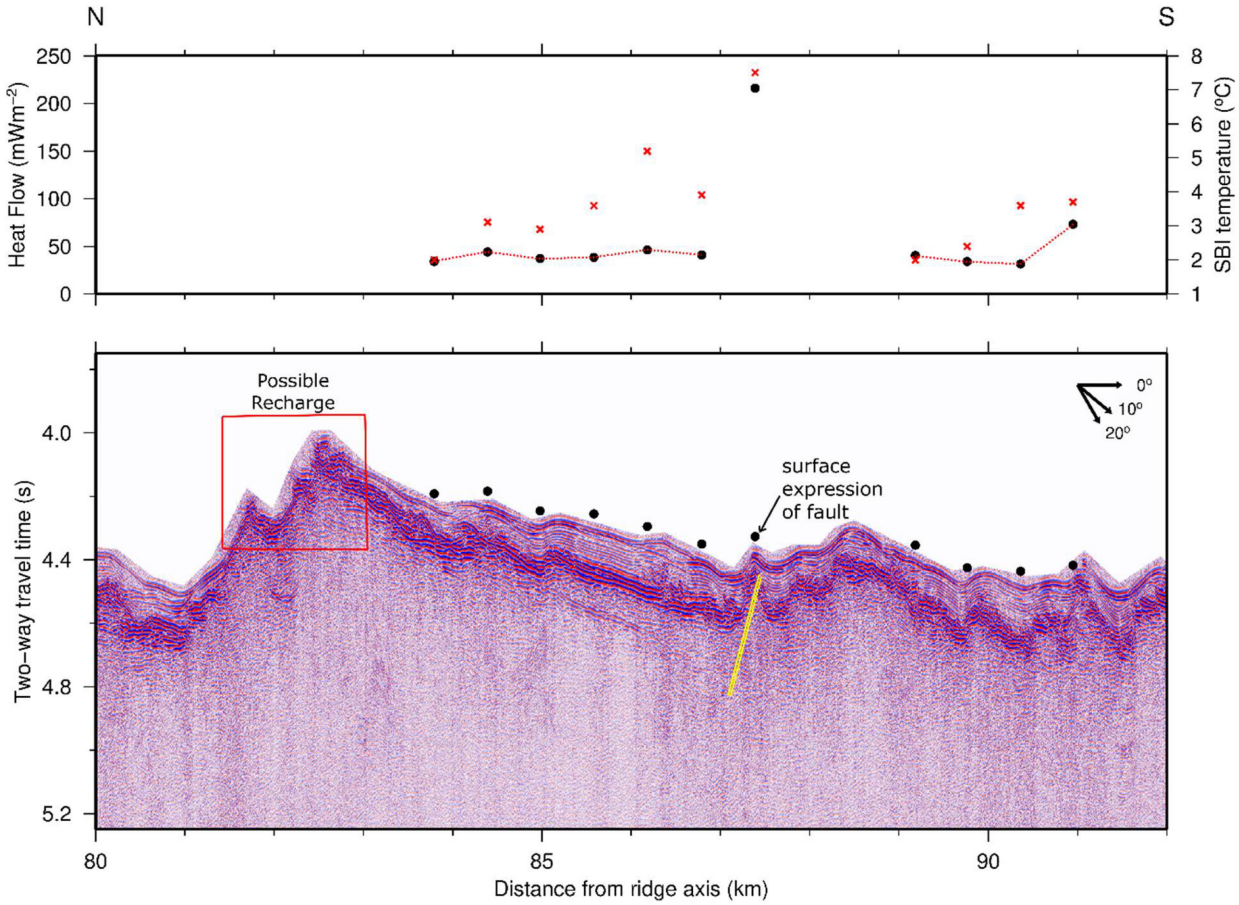

Figure 7. Site PB03 (2.6 Ma). (a) 11 heat-flow measurements (black circles) as a function of distance from the CRR axis. The red crosses show SBI temperatures at each heat-flow measurement. (b) Pre-stack time-migrated seismic image of PB03 plotted as in Fig. 6. The yellow parallel lines indicate possible fault location and the black arrow points at surface expression of possible fault. The red box indicates possible recharge area. N, North; S, South. Note: faults are shown only where there is circumstantial evidence of enhanced heat flow which is interpreted as that caused by focused flow along a fault.

eq. (C2), with $q_b = 322$ mW m^{-2}, we calculate T_{sp} to be in the range of 25–50 °C accounting for thermal conductivity difference between sediment and basement. The estimated temperature of the fluid discharging through the fault is considerably higher than T_{SBI}^{obs}, suggesting that the fault may be tapping warmer fluids from below the upper basement.

Advective heat transfer at site PB04 stems from different environments, and it is not possible to determine the heat loss and the fluid discharge temperature from each site independently. Given the low value of conductive heat flux in group C, we suggest that most of the advective loss is associated with outcrop to outcrop circulation.

4.4 Heat-flow site PB05

The seven heat-flow measurements at this site (Table 1) have a mean of 14 mW m^{-2}. The crustal age of 4.5 Ma corresponds to a predicted heat flow (eq. 1a) $q_b = 241$ mW m^{-2}, indicating a deficit of about 0.94. Thus $q_{adv} \sim 230$ mW m^{-2}. The average sediment thickness ≈ 120 m except above the large basement mound (Fig. 9b), where h_s varies between 0 and 80 m. From the two-way traveltime data, the basement high is approximately 1 km from the base of the sediment layer to the north where the heat-flow data were obtained. The sediment thickness at the top of the mound and along its southern flank is negligible. Heat flow increases slightly towards the topographic basement high (Fig. 9), suggesting that heat maybe being transferred by advection within it.

If basal heat flow through the basement is 241 mW m^{-2}, the conductive temperature at the base of the basement high (∼1 km) would be ≈20 °C, whereas the conductive temperature at the base of the nearby sediment would be ≈40 °C. This strong lateral temperature gradient between the sediments and the basement high would drive fluid upwards through the basement. From the scale analysis, the vertical velocity is given by

$$u_z \sim \frac{\alpha g k \Delta T}{\nu}. \quad (4)$$

Because we do not know whether the advection is sub- or supercritical, we assume that the permeability corresponds to $Ra = Ra_c$ in a 550 m thick aquifer. From Fig. 5, this value is ≈4 ×10^{-13} m^2, yielding $u_z \approx 1.6 \times 10^{-8}$ m s^{-1} assuming a mean $\Delta T = 40$ °C driving the flow. If the fluid rising through the basement high exits the sediment-free part of the mound at a typical diffuse flow temperature ≈10 °C (Fisher & Harris 2010), $q_{adv} = \rho_f c_f u_z \Delta T \approx 640$ mW m^{-2}, which is approximately three times greater than the mean heat-flow deficit of ≈230 mW m^{-2}. In order for the total advective heat output through the basement high to balance the observed advective heat flux, the area of advective heat loss in the crust surrounding the basement high would thus need to be approximately three times

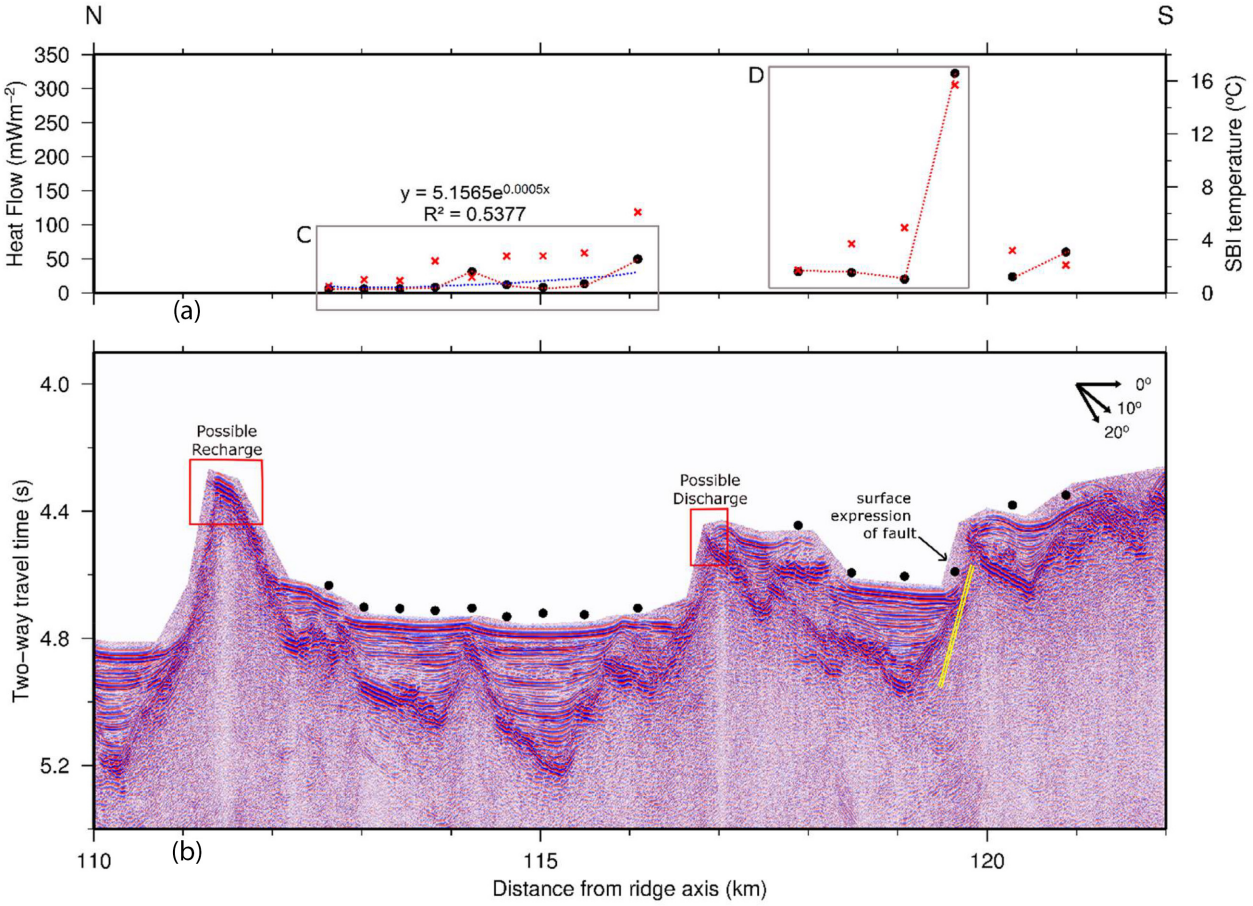

Figure 8. Site PB04 (3.5 Ma). (a) 15 heat-flow measurements (black circles) as a function of distance from the CRR axis. The red crosses show SBI temperatures at each heat-flow measurement. The grey boxes indicate sets C and D discussed in the text. The blue dashed line shows best-fitting exponential function (refer eq. B2) which is the solution to eq. (B1), enabling the estimation of volumetric flow rate per unit length. R^2 shows the goodness of fit of the exponential equation. (b) Pre-stack time-migrated seismic image of PB04 plotted as in Fig. 6. The yellow parallel lines indicate possible fault location and the black arrow points at surface expression of possible fault. The red boxes indicates possible recharge and discharge areas. N, North; S, South. Note: faults are shown only where there is circumstantial evidence of enhanced heat flow which is interpreted as that caused by focused flow along a fault.

the area through which advective heat is lost through the basement high. Alternatively, heat advection through the basement high resulting from the lateral temperature gradient may be subcritical. The permeability of the basement may thus be an order of magnitude, or more, less than estimated assuming $Ra \approx Ra_c$.

4.5 Heat-flow site PB06

Site PB06 (Fig. 10) consists of 15 measurements in 5.7 Ma crust with a mean observed heat flow of 235 mW m^{-2}, slightly higher than the predicted heat flow of 214 mW m^{-2} (Table 1). The sediment thickness averages 145 m, burying the basement. The relative agreement between the observed and the predicted heat flows is consistent with the thick and continuous sediment cover. The observed heat flow varies from 899 mW m^{-2} over a basement high to 90 mW m^{-2} over the basement low (Fig. 10). This variation is greater than can be accounted for with conductive refraction (Von Herzen 2004). The mean observed basement temperature, $< \Delta T_{\rm SBI}^{\rm obs} > \approx 26\ ^\circ$C is that expected for this crustal age and sediment thickness, but the variability is larger than can be accounted for with conductive heat flow. Importantly, the SBI temperature is not constant but varies substantially with sediment thickness variations; over the basement high, the sediment thickness is 19 m and $\Delta T_{\rm SBI}^{\rm obs}$ is significantly higher (18.8 °C) than predicted (4.4 °C). Over the basement low, the sediment thickness is 226 m and $\Delta T_{\rm SBI}^{\rm obs}$ is significantly lower (29 °C) than predicted (52.7 °C). The variability in both heat flow and SBI temperature suggests on going hydrothermal circulation, but because the SBI temperature is not homogenized, convection must be subcritical or only slightly supercritical.

These results suggest upward advective fluid flow in the basement high and downward advective flow in the basement low. These results are similar to those near Hole 504B where heat-flow highs occur over bathymetric ridges, basement highs and regions of thin sediment cover, with lows occur over basement lows and regions of thick sediment cover (Fisher *et al.* 1990, 1994). Because of the complex interplay of these factors it is difficult to quantify fluid flow rates and basement permeability, but the lateral temperature gradients induced by variations in basement topography and sediment thickness may result in circulation at subcritical Rayleigh numbers. Subcritical convection is consistent with the broad spectrum of temperatures at the SBI. Assuming that convection in a 550 m thick layer of basement extrusives is at or near the critical number for Rayleigh convection, gives the mean permeability at PB06 of $\sim 5 \times 10^{-13}$ m^2.

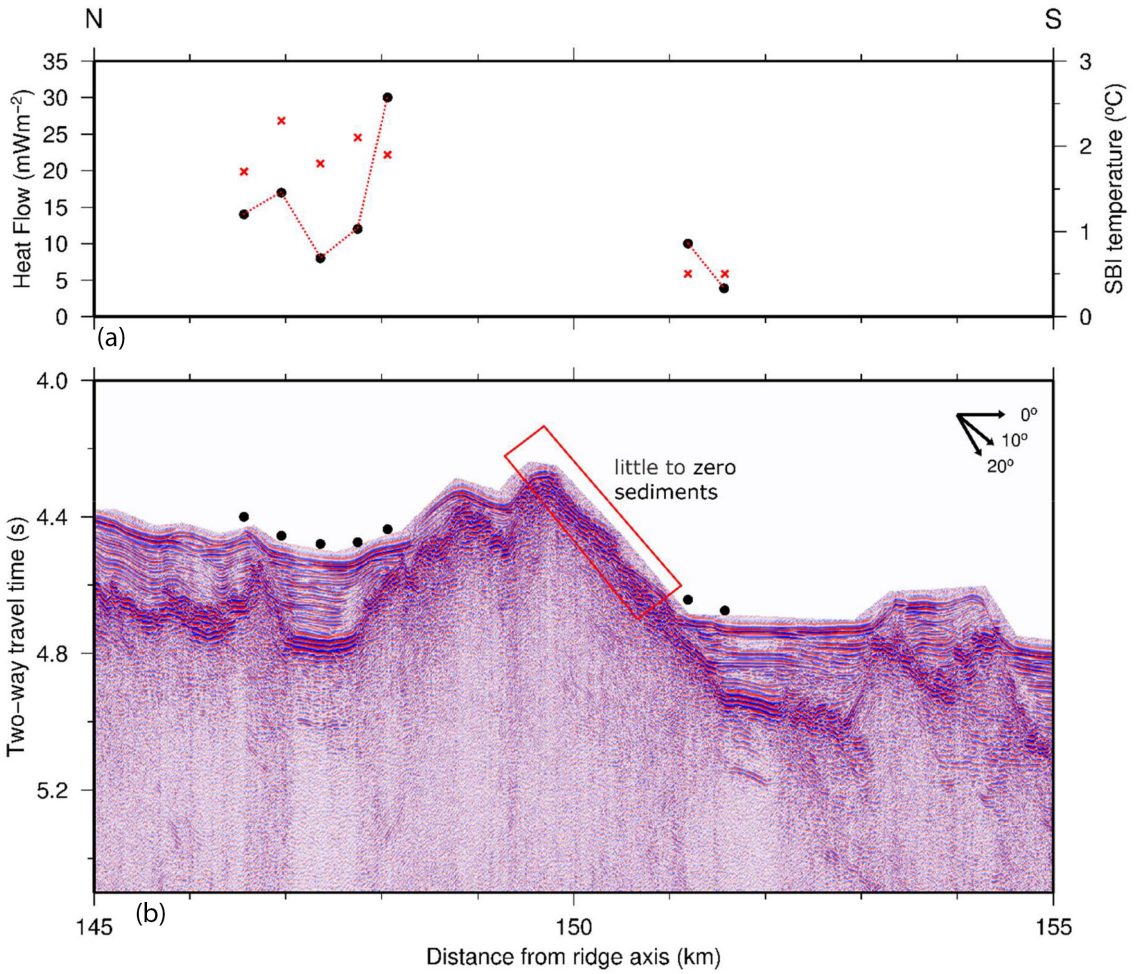

Figure 9. Site PB05 (4.5 Ma). (a) 7 heat-flow measurements (black circles) as a function of distance from the CRR axis. The red crosses show SBI temperatures at each heat-flow measurement. (b) Pre-stack time-migrated seismic image of PB05 plotted as in Fig. 6. The red box indicates an area of little to no sediment. N, North; S, South. Note: faults are shown only where there is circumstantial evidence of enhanced heat flow which is interpreted as that caused by focused flow along a fault.

5 DISCUSSION AND CONCLUSIONS

The 67 new conductive heat-flow measurements collected on the southern flank of the CRR crust between ≈1.6 and ≈5.7 Ma, together with legacy data, provide important insights into types and patterns of hydrothermal circulation and advective heat loss from young crust. Comparison between the observed heat flow and the predicted half-space lithospheric cooling model yields a mean heat-flow deficit of ≈ 70 per cent that is attributed primarily to advective heat transport. Detailed analysis of each site, however, suggests that the magnitude of advective heat transfer (Table 3) is not a simple function of crustal age. These results provide new insights into hydrothermal circulation mechanisms as conductive heat flow approaches the predicted heat-flow curve (Fig. 1).

Our analysis indicates that between sites PB02 and PB04 supercritical Rayleigh convection tends to homogenize the basement temperature distribution. Outcrop-to-outcrop circulation (PB02, PB04) and fluid flow through faults (PB03 and PB04), which are superimposed on the Rayleigh convection regime, act to cool the basement by advecting heat to the ocean (Fig. 3). At PB05, advective heat loss likely occurs as a result of subcritical convective flow driven by a significant lateral mean temperature difference between the basement high and surrounding sediments. The advected heat exits through a sediment-free part of the basement high. At PB06, however, there is little evidence of advective heat exchange between the basement and ocean. Thermal convection in the basement is likely subcritical, driven by differences in basement topography (Figs 3 and 10).

We constructed relatively simple mathematical models and/or used the scale analysis for sites PB02–PB05 to understand advective heat flow and estimate the permeability of the upper crust. At PB06 we estimated permeability assuming $Ra \approx Ra_c$. Table 3 lists the estimated permeability at each site, along with that for 6.9 Ma crust near Hole 504B. The results of the scale analysis and mathematical modelling points to an order magnitude difference in permeability between the upper 150 m and that of the entire Layer 2A, estimated to be 550 m thick (Table 3). Moreover, the results show that permeability does not decrease monotonically with age, as might be expected from water–rock reactions that tend to fill fracture and pore spaces.

The estimates of basement permeability derived here are not a monotonic function of age. The permeability at site PB03 which has an age of 2.6 Ma appears to be less than at adjacent sites that are both older and younger. Moreover, the estimated crustal permeability drops significantly between PB04 and PB05 (3.5–4.5 Ma); and it appears to increase again at PB06. At Hole 504B at 6.9 Ma crust,

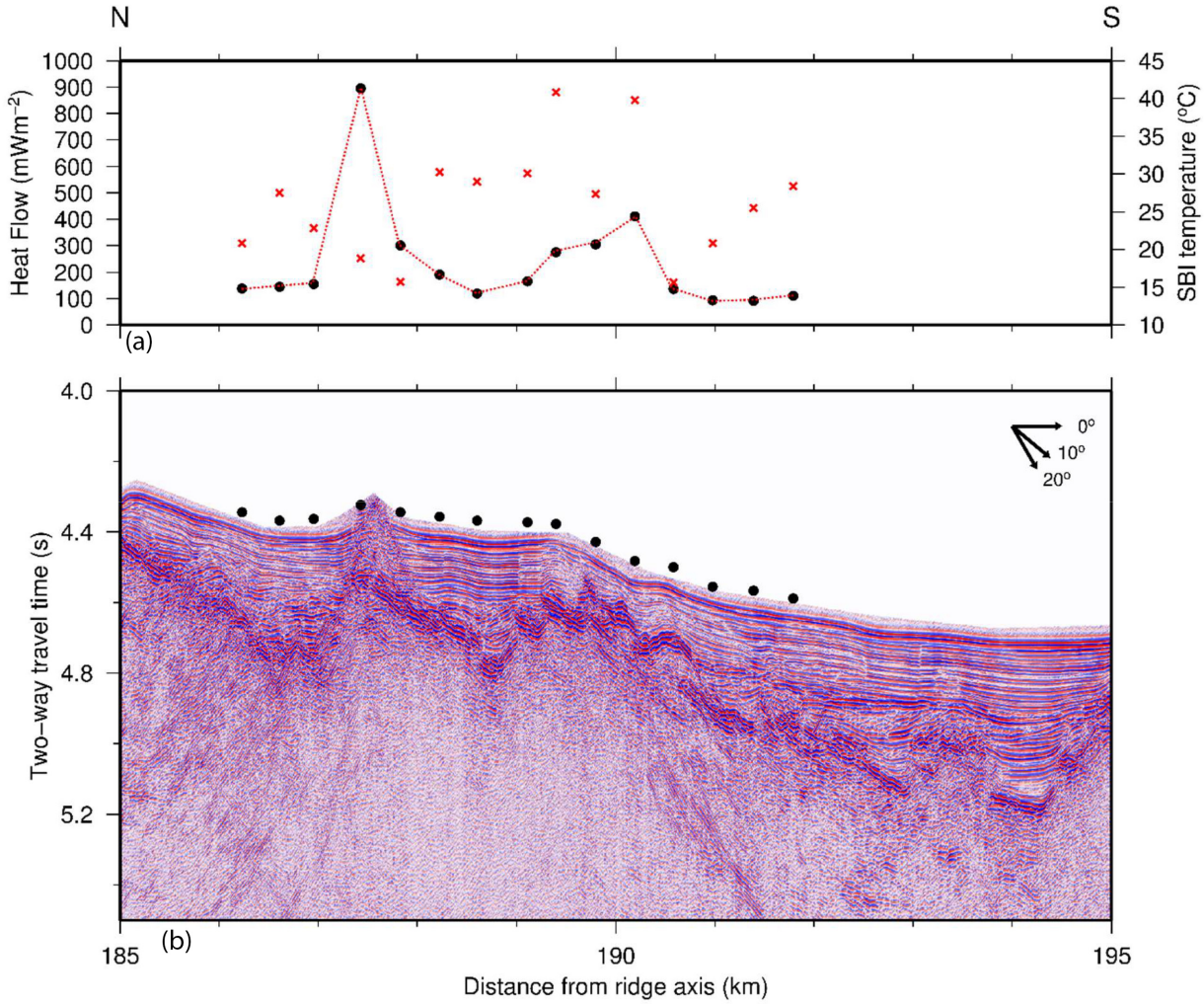

Figure 10. Site PB06 (5.7 Ma). (a) 15 heat-flow measurements (black circles) as a function of distance from the CRR axis. The red crosses show SBI temperatures at each heat-flow measurement. (b) Pre-stack time-migrated seismic image of PB06 plotted as in Fig. 6. N, North; S, South. Note: faults are shown only where there is circumstantial evidence of enhanced heat flow which is interpreted as that caused by focused flow along a fault.

packer measurements yield permeabilities in the range of 10^{-13}–10^{-14} m^2 (Anderson & Zoback 1982; Fisher *et al.* 1990) and flow-based determinations produce upper basement permeabilities of 1–5×10^{-14} m^2 (Becker *et al.* 2004). At Hole 896A, located 1 km from Hole 504B, drill-string packer measurements (Becker 1996) and flow-based determinations (Becker *et al.* 2004) give upper basement permeabilities of 1–4×10^{-13} m^2 and lower basement permeability of 2×10^{-14} m^2. However, the near uniformity of the basement temperature between Hole 504B, Hole 896A and Holes 677, 678, despite large differences in sediment thickness, suggests vigorous convection in the upper crustal layer. Davis *et al.* (2004) suggest a model-based regional-scale permeability of $\sim 10^{-9}$ m^2 in the upper 100 m. The substantial transition to decreased permeabilities from 3.5 to 4.5 Ma and a continued decrease in permeability in the shallow crust at 6.9 Ma suggest that the evolution of crustal permeability may not be simply correlated with crustal age.

The variability in estimated crustal permeabilities is similar to the variability seen in tomographic models of seismic *P*-wave velocity in Layer 2A of the ocean crust (Wilson *et al.* 2018). The upper oceanic crust older than about 5.7 Ma consistently shows a higher seismic velocity that is interpreted to be a result of porosity reduction (Gregory *et al.* 2019; Wilson *et al.* 2019). The crust younger than 5.7 Ma can be segmented into regions characterized by a combination of basement roughness, seismic velocity of Layers 2A and 2B, and ages determined from reinterpretation of magnetic anomaly data (Wilson *et al.* 2019). Taken together, these characteristics suggest that the magma supply has waxed and waned with time. Heat-flow measurements at sites PB02 and PB03 lie in a region where the tomography model indicates a lower velocity Layer 2A, which is consistent with the relatively high permeability estimated for this region. Sites PB04 and PB05 are located in a region of variable *P*-wave velocities in Layer 2A. Wilson *et al.* (2019) suggest that this region has formed during a period of slower spreading, <35 mm yr^{-1} half-rate, with enhanced faulting accommodating part of the extension. This may explain the rapid change in estimated permeability. Site PB06 and Hole 504B lie within the transition to significantly faster Layer 2A velocities, which are interpreted to indicate an earlier phase of magma-dominated spreading.

The models used to analyse the heat-flow data along the seismic line from crustal ages of $\approx$1.6 to $\approx$5.7 Ma are necessarily simplified. In addition, the models all assume 2-D flow parallel to the spreading direction, whereas enhanced permeability may be aligned parallel to the ridge (Fisher *et al.* 2008; Neira *et al.* 2016). Outcrop-to-outcrop flow may also be 3-D (Winslow & Fisher 2015; Winslow *et al.* 2016),

and fault-controlled flow may be both along and perpendicular to the plane of the fault (e.g. Johnson *et al.* 1993; Lowell 2017). The permeability values estimated for the various sites represent bulk average permeabilities. The estimated values obtained are large, indicating that the permeability is probably fracture controlled, and the actual flow paths may be both anisotropic and defined by a few major fractures rather than by the Darcy flow as used here.

Fig. 1(b) shows that heat flow at sites PB02 through PB05 lies well below the predicted cooling curve but begin climbing towards the cooling curve at ≈4.5 Ma, essentially reaching the curve at 5.7 Ma. This result is in contrast with the global data set (Fig. 1a) where heat flow coincides with the predicted heat flow at ≈65 ± 10 Ma. Stein & Stein (1994) argue that the coincidence of conductive heat flow with the predicted cooling curve suggests that hydrothermal circulation is weak as a result of decreasing crustal permeability rather than a result of increasing sediment thickness burying basement rock. This study, where heat flow coincides with the cooling curve at a much younger crustal age of ≈5.7 Ma, however, indicates that the alignment of heat flow with the predicted curve may be a function of original permeability at the time of crustal formation or reduction of permeability, which may result from mineral precipitation as well as mode of crustal generation, as well as sediment accumulation. The data at PB05 and PB06 indicate that a decline in crustal permeability results in subcritical or weakly supercritical convection, driven largely by basement topography. The relatively thick, low permeability sediment cover over crust older than about 5.7 Ma inhibits advective heat transfer to the ocean (Fig. 3). This is similar to the JDFR flank where thick sediment cover also inhibits advective heat loss from young crust (Davis *et al.* 1997, 1999; Spinelli & Fisher 2004; Hutnak *et al.* 2006).

The results of studies at young crust thus suggest that permeability, sediment thickness, topographical structure and variations in tectonic and magmatic activities with age all affect hydrothermal circulation in the oceanic crust in a complex interconnected fashion. This interconnectedness is more site specific than that can be constrained by global data sets and models simply as a function of age. Increased understanding of crustal evolution and hydrothermal circulation will come as individual spreading systems are analysed that include details of crustal creation, tectonic evolution, water rock reactions, sedimentation and age.

ACKNOWLEDGEMENTS

The authors would like to thank the thorough and constructive reviews from Dr Keir Becker and one other anonymous reviewer that helped improve this manuscript. This research was supported in part by NSF Grants OCE 1353114 and 1558797 to RPL and Grants NSF OCE 1353003 and 1558824 to RNH. The NERC OSCAR project grant NE/I027010/1 (Hobbs & Peirce 2015) underpinned this work. The authors would like to thank the officers, crew, technicians and science party on board the RRS James Cook during cruises JC112, JC113 and JC114. The MCS data were processed using GNS Globe Claritas at Durham University. The swath bathymetry was cleaned and processed using QPS Fledermaus by Gavin Haughton from the National Oceanographic Centre and Emma Gregory from Durham University. Yang Li, Durham University, UK, provided the Monte Carlo Matlab code for calculation of uncertainties. The heat-flow data have been placed on the IEDA data portal, doi: http://dx.doi.org/10.1594/IEDA/324068, seismic data are available on request through the British Oceanographic Data Center or the author RWH.

REFERENCES

Alt, J.C., 1995. Sulfur isotopic profile through the oceanic crust: sulfur mobility and seawater-crustal sulfur exchange during hydrothermal alteration, *Geology,* **23**(7), 585–588.

Anderson, B.W., Coogan, L.A. & Gillis, K.M., 2012. The role of outcrop-to-outcrop fluid flow in off-axis oceanic hydrothermal systems under abyssal sedimentation conditions, *J. geophys. Res.,* **117**(B5), doi:10.1029/2011JB009052.

Anderson, R.N. & Hobart, M.A., 1976. The relation between heat flow, sediment thickness, and age in the eastern Pacific, *J. geophys. Res.,* **81**(17), 2968–2989.

Anderson, R.N. & Zoback, M.D., 1982. Permeability, underpressures, and convection in the oceanic crust near the Costa Rica Rift, eastern equatorial Pacific, *J. geophys. Res.,* **87**(B4), 2860–2868.

Baker, P.A., Stout, P.M., Kastner, M. & Elderfield, H., 1991. Large-scale lateral advection of seawater through oceanic crust in the central equatorial Pacific, *Earth planet. Sci. Lett.,* **105**(4), 522–533.

Becker, K., 1985. Large-scale electrical resistivity and bulk porosity of the oceanic crust, Deep Sea Drilling Project Hole 504B, Costa Rica Rift, Anderson, R.N., in *Initial Reports DSDP, Leg 83, Balboa to Balboa, Panama,* US Govt. Printing Office; UK distributors, IPOD Committee, NERC.

Becker, K., 1996. Permeability measurements in Hole 896A and implications for the lateral variability of upper crustal permeability at Sites 504 and 896, *Proc. Ocean Drill. Program, Sci. Results,* **148,** 353–364.

Becker, K. & Davis, E.E., 2004. In situ determinations of the permeability of the igneous oceanic crust, in *Hydrogeology of the Oceanic Lithosphere,* pp. 189–224, eds Davis, E.E. & Elderfield, H., Cambridge Univ. Press.

Becker, K., Davis, E.E. & Spiess, F.N., 2004. Temperature and video logs from the upper oceanic crust, Holes 504B and 896A, Costa Rica Rift flank: implications for the permeability of upper oceanic crust, *Earth planet. Sci. Lett.,* **222**(3-4), 881–896.

Becker, K., Langseth, M.G., Von Herzen, R.P. & Anderson, R., 1983. Deep crustal geothermal measurements, Hole 504B, Costa Rica Rift, *J. geophys. Res.,* **88,** 3447–3457.

Becker, K., Sakai, H., Adamson, A.C., Alexandrovich, J., Alt, J.C., Anderson, R.N. & Ishizuka, H., 1989. Drilling deep into young oceanic crust, Hole 504B, Costa Rica Rift, *Rev. Geophys.,* **27**(1), 79–102.

Carlson, R.L., 2011. The effect of hydrothermal alteration on the seismic structure of the upper oceanic crust: evidence from Holes 504B and 1256D, *Geochem. Geophys. Geosyst.,* **12**(9), doi:10.1029/2011GC003624.

Carlson, R.L., 2014. The effects of alteration and porosity on seismic velocities in oceanic basalts and diabases, *Geochem. Geophys. Geosyst.,* **15**(12), 4589–4598.

Carslaw, H.S. & Jaeger, J.C., 1959. *Conduction of Heat in Solids,* 2nd edn, Clarendon Press.

Cherkaoui, A.S., Wilcock, W.S., Dunn, R.A. & Toomey, D.R., 2003. A numerical model of hydrothermal cooling and crustal accretion at a fast spreading mid-ocean ridge, *Geochem. Geophys. Geosyst.,* **4**(9), doi:10.1029/2001GC000215.

Craft, K.L. & Lowell, R.P., 2009. A boundary layer model for submarine hydrothermal heat flows at on-axis and near-axis regions, *Geochem. Geophys. Geosyst.,* **10**(12), doi:10.1029/2009GC002707.

Davies, J.H. & Davies, D.R., 2010. Earth's surface heat flux, *Solid Earth,* **1**(1), 5–24.

Davis, E.E., Becker, K. & He, J., 2004. Costa Rica Rift revisited: constraints on shallow and deep hydrothermal circulation in young oceanic crust, *Earth planet. Sci. Lett.,* **222**(3-4), 863–879.

Davis, E.E., Chapman, D.S., Wang, K., Villinger, H., Fisher, A.T., Robinson, S.W. & Becker, K., 1999. Regional heat flow variations across the sedimented Juan de Fuca Ridge eastern flank: constraints on lithospheric cooling and lateral hydrothermal heat transport, *J. geophys. Res.,* **104**(B8), 17 675–17 688 .

Davis, E.E., Fisher, A.T., Firth, J.V., Staff Scientist, L., Fox, P.J., Allan, J. & Home, O.D.P., 1997. Hydrothermal circulation in the oceanic crust: eastern flank of the Juan de Fuca Ridge, *Proc. Ocean Drill. Program, Initial Rep.,* **168,** 1–470.

Davis, E.E., Wang, K., Becker, K., Thomson, R.E. & Yashayaev, I., 2003. Deep-ocean temperature variations and implications for errors in seafloor heat flow determinations, *J. geophys. Res.,* **108**(B1), doi:10.1029/2001JB001695.

Elderfield, H. & Schultz, A., 1996. Mid-ocean ridge hydrothermal fluxes and the chemical composition of the ocean, *Annu. Rev. Earth Planet. Sci.,* **24**(1), 191–224.

Elder, J.W., 1965. Physical processes in geothermal areas, in *Terrestrial Heat Flow,* Geophysical Monograph Series, Vol. **8,** pp. 211–239, ed. Lee, W.H.K., AGU.

Embley, R.W., Hobart, M.A., Anderson, R.N. & Abbott, D., 1983. Anomalous heat flow in the northwest Atlantic: a case for continued hydrothermal circulation in 80-MY crust, *J. geophys. Res.,* **88**(B2), 1067–1074.

Fisher, A.T., 1998. Permeability within basaltic oceanic crust, *Rev. Geophys.,* **36**(2), 143–182.

Fisher, A.T., 2003. Geophysical constraints on hydrothermal circulation: observations and models, in *Energy and Mass Transfer in Marine Hydrothermal Systems,* Vol. **89,** pp. 29–52, eds Halbach, P.E., Tunnicliffe, V. & Hein, J.R., Dahlem University Press.

Fisher, A.T. & Becker, K., 2000. Channelized fluid flow in oceanic crust reconciles heat-flow and permeability data, *Nature,* **403**(6765), 71–74.

Fisher, A.T., Becker, K., Narasimhan, I.T.N., Langseth, M.G. & Mottl, M.J., 1990. Passive, off-axis convection through the southern flank of the Costa Rica Rift, *J. geophys. Res.,* **95**(B6), 9343–9370.

Fisher, A.T., Becker, K. & Narasimhan, T.N., 1994. Off-axis hydrothermal circulation: parametric tests of a refined model of processes at Deep Sea Drilling Project/Ocean Drilling Program site 504, *J. geophys. Res.,* **99**(B2), 3097–3121.

Fisher, A.T., Davis, E.E. & Becker, K., 2008. Borehole-to-borehole hydrologic response across 2.4 km in the upper oceanic crust: implications for crustal-scale properties, *J. geophys. Res.,* **113,** B07106, doi:10.1029/2007JB005447.

Fisher, A.T., Davis, E.E., Hutnak, M., Spiess, V., Zühlsdorff, L., Cherkaoui, A. & Mottl, M.J., 2003b. Hydrothermal recharge and discharge across 50 km guided by seamounts on a young ridge flank, *Nature,* **421**(6923), 618–621.

Fisher, A.T. & Harris, R.N., 2010. Using seafloor heat flow as a tracer to map subseafloor fluid flow in the ocean crust, *Geofluids,* **10**(1-2), 142–160.

Fisher, A.T. & Von Herzen, R.P., 2005. Models of hydrothermal circulation within 106 Ma seafloor: constraints on the vigor of fluid circulation and crustal properties, below the Madeira Abyssal Plain, *Geochem. Geophys. Geosyst.,* **6**(11), doi:10.1029/2005GC001013.

Fisher, A.T. *et al.*, 2003a. Abrupt thermal transition reveals hydrothermal boundary and role of seamounts within the Cocos Plate, *Geophys. Res. Lett.,* **30**(11), doi:10.1029/2002GL016766.

Gregory, E.P.M., Hobbs, R.W., Peirce, C. & Wilson, D.J., 2019. 2B or not 2B? – a terminology-independent proxy for characterising the extrusive-intrusive transition in magmatic oceanic crust, *Geochem. Geophys. Geosyst.,* submitted.

Hasenclever, J., Theissen-Krah, S., Rüpke, L.H., Morgan, J.P., Iyer, K., Petersen, S. & Devey, C.W., 2014. Hybrid shallow on-axis and deep off-axis hydrothermal circulation at fast-spreading ridges, *Nature,* **508**(7497), 508–512.

Hasterok, D., 2013. A heat flow based cooling model for tectonic plates, *Earth planet. Sci. Lett.,* **361,** 34–43.

Heberling, C., Lowell, R.P., Liu, L. & Fisk, M.R., 2010. Extent of the microbial biosphere in the oceanic crust, *Geochem. Geophys. Geosyst.,* **11**(8), Q08003, doi:10.1029/2009GC002968.

Hobart, M.A., Langseth, M.G. & Anderson, R.N., 1985. A geothermal and geophysical survey on the south flank of the Costa Rica Rift: sites 504 and 505, *Initial Rep. Deep Sea Drill. Proj.,* **83**(APR), 379–404.

Hobbs, R.W. & Peirce, C., 2015. RRS James Cook JC114 Cruise Report.

Huber, J.A., Butterfield, D.A. & Baross, J.A., 2003. Bacterial diversity in a subseafloor habitat following a deep-sea volcanic eruption, *FEMS Microbiol. Ecol.,* **43**(3), 393–409.

Hutchison, I., 1985. The effects of sedimentation and compaction on oceanic heat flow, *Geophys. J. Int.,* **82**(3), 439–459.

Hutnak, M. & Fisher, A.T., 2007. Influence of sedimentation, local and regional hydrothermal circulation, and thermal rebound on measurements of seafloor heat flux, *J. geophys. Res.,* **112**(B12), doi:10.1029/2007JB005022.

Hutnak, M., Fisher, A.T., Harris, R., Stein, C., Wang, K., Spinelli, G. & Silver, E., 2008. Large heat and fluid fluxes driven through mid-plate outcrops on ocean crust, *Nat. Geosci.,* **1**(9), 611–614.

Hutnak, M., Fisher, A.T., Zühlsdorff, L., Spiess, V., Stauffer, P.H. & Gable, C.W., 2006. Hydrothermal recharge and discharge guided by basement outcrops on 0.7–3.6 Ma seafloor east of the Juan de Fuca Ridge: observations and numerical models, *Geochem. Geophys. Geosyst.,* **7**(7), Q7002, doi:10.1029/2006GC001242.

Hyndman, R.D., Davis, E.E. & Wright, J.A., 1979. The measurement of marine geothermal heat flow by a multipenetration probe with digital acoustic telemetry and in situ thermal conductivity, *Mar. Geophys. Res.,* **4**(2), 181–205.

Jarrard, R.D., Abrams, L.J., Pockalny, R., Larson, R.L. & Hirono, T., 2003. Physical properties of upper oceanic crust: Ocean Drilling Program Hole 801C and the waning of hydrothermal circulation, *J. geophys. Res.,* **108**(B4), doi:10.1029/2001JB001727.

Johnson, H.P., Becker, K. & Von Herzen, R., 1993. Near-axis heat flow measurements on the northern Juan de Fuca Ridge: implications for fluid circulation in oceanic crust, *Geophys. Res. Lett.,* **20**(17), 1875–1878.

Kolandaivelu, K.P., Harris, R.N., Lowell, R.P., Alhamad, A., Gregory, E.P. & Hobbs, R.W., 2017. Analysis of a conductive heat flow profile in the Ecuador Fracture Zone, *Earth planet. Sci. Lett.,* **467,** 120–127.

Langseth, M.G., Becker, K., Von Herzen, R.P. & Schultheiss, P., 1992. Heat and fluid flux through sediment on the western flank of the Mid-Atlantic Ridge: a hydrogeological study of North Pond, *Geophys. Res. Lett.,* **19**(5), 517–520.

Langseth, M.G., Cann, J.R., Natland, J.H. & Hobart, M., 1983. Geothermal phenomenon at the Costa Rica Rift: background and objectives for drilling at Deep Seas Drilling Project sites 501, 504, and 505, *Initial Rep. Deep Sea Drill. Proj.,* **69**(MAY), 5–30.

Langseth, M.G. & Herman, B.M., 1981. Heat transfer in the oceanic crust of the Brazil Basin, *J. geophys. Res.,* **86**(B11), 10 805–10 819.

Langseth, M.G., Mottl, M.J., Hobart, M.A. & Fisher, A., 1988. The distribution of geothermal and geochemical gradients near Site 501/504: implications for hydrothermal circulation in the oceanic crust, *Proc. Ocean Drill. Program, Initial Rep.,* **111,** 23–32.

Langseth, M.G. & Von Herzen, R.P., 1970. Heat flow through the floor of the world oceans, *The Sea,* **4**(part 1), 299–352.

Lister, C.R.B., 1972. On the thermal balance of a mid-ocean ridge, *Geophys. J. Int.,* **26**(5), 515–535.

Lister, C.R.B., 1982. "Active" and "passive" hydrothermal systems in the oceanic crust: predicted physical conditions, in *The Dynamic Environment of the Ocean Floor,* pp. 441–470, eds Fanning, K. & Manheim, F.T., D.C. Hearth.

Lonsdale, P. & Klitgord, K.D., 1978. Structure and tectonic history of the eastern Panama Basin, *Bull. geol. Soc. Am.,* **89**(7), 981–999.

Lowell, R.P., 1975. Circulation in fractures, hot springs, and convective heat transport on mid-ocean ridge crests, *Geophys. J. Int.,* **40**(3), 351–365.

Lowell, R.P., 2017. A fault-driven circulation model for the Lost City Hydrothermal Field, *Geophy. Res. Lett.,* **44**(6), 2703–2709.

Macdonald, K.C., 1982. Mid-ocean ridges: fine scale tectonic, volcanic and hydrothermal processes within the plate boundary zone, *Annu. Rev. Earth Planet. Sci.,* **10**(1), 155–190.

Neira, N.M., Clark, J.F., Fisher, A.T., Wheat, C.G., Haymon, R.M. & Becker, K., 2016. Cross-hole tracer experiment reveals rapid fluid flow and low effective porosity in the upper oceanic crust, *Earth planet. Sci. Lett.,* **450,** 355–365.

Nield, D.A., 1968. Onset of thermohaline convection in a porous medium, *Water Resour. Res.,* **4**(3), 553–560.

Parsons, B. & Sclater, J.G., 1977. An analysis of the variation of ocean floor bathymetry and heat flow with age, *J. geophys. Res.,* **82**(5), 803–827.

Qiuming, C., 2016. Fractal density and singularity analysis of heat flow over ocean ridges, *Sci. Rep.,* **6,** 19167, doi:10.1038/srep19167.

Salisbury, M.H., Christensen, N.I., Becker, K. & Moos, D., 1985. The velocity structure of Layer 2 at Deep Sea Drilling Project Site 504 from logging and laboratory experiments, 529–539.
Sclater, J., Jaupart, C. & Galson, D., 1980. The heat flow through oceanic and continental crust and the heat loss of the Earth, *Rev. Geophys.,* **18**(1), 269–311.
Spinelli, G.A. & Fisher, A.T., 2004. Hydrothermal circulation within topographically rough basaltic basement on the Juan de Fuca Ridge flank, *Geochem. Geophys. Geosyst.,* **5**(2), doi:10.1029/2003GC000616.
Spinelli, G.A., Giambalvo, E.R. & Fisher, A.T., 2004. Sediment permeability, distribution, and influence on fluxes in oceanic basement, eds Davis, E.E. & Elderfield, H., *in Hydrogeology of the Oceanic Lithosphere,* Cambridge Univer. Press, New York, p. 151–188.
Spinelli, G.A. & Harris, R.N., 2011. Effects of the legacy of axial cooling on partitioning of hydrothermal heat extraction from oceanic lithosphere, *J. geophys. Res.,* **116**(B9), B09102, doi:10.1029/2011JB008248.
Stein, C.A. & Stein, S., 1992. A model for the global variation in oceanic depth and heat flow with lithospheric age, *Nature,* **359**(6391), 123–129.
Stein, C.A. & Stein, S., 1994. Constraints on hydrothermal heat flux through the oceanic lithosphere from global heat flow, *J. geophys. Res.,* **99**(B2), 3081–3095.
Stein, J.S. & Fisher, A.T., 2001. Multiple scales of hydrothermal circulation in Middle Valley, northern Juan de Fuca Ridge: physical constraints and geologic models, *J. geophys. Res.,* **106**(B5), 8563–8580.
Theissen-Krah, S., Iyer, K., Rüpke, L.H. & Morgan, J.P., 2011. Coupled mechanical and hydrothermal modeling of crustal accretion at intermediate to fast spreading ridges, *Earth planet. Sci. Lett.,* **311**(3-4), 275–286.
Villinger, H. & Davis, E.E., 1987. A new reduction algorithm for marine heat flow measurements, *J. geophys. Res.,* **92**(B12), 12 846–12 856.
Von Herzen, R.P., 2004. Geothermal evidence for continuing hydrothermal circulation in older (>60 Ma) ocean crust, in *Hydrogeology of the Oceanic Lithosphere,* pp. 414–450, eds Davis, E.E. & Elderfield, H., Cambridge Univ. Press.
Wheat, C.G., Mottl, M.J., Fisher, A.T., Kadko, D., Davis, E.E. & Baker, E., 2004. Heat flow through a basaltic outcrop on a sedimented young ridge flank, *Geochem. Geophys. Geosyst.,* **5**(12), doi:10.1029/2004GC000700.
Williams, D.L. & Von Herzen, R.P., 1974. Heat loss from the Earth: new estimate, *Geology,* **2**(7), 327–328.
Wilson, D.J., Robinson, A.H., Hobbs, R.W., Peirce, C. & Funnell, M.J., 2019. Does intermediate spreading-rate oceanic crust result from episodic transition between magmatic and magma-dominated, faulting-enhanced spreading? – The Costa Rica rift examaple, *Geophys. J. Int.,* **218,** p. 1617–1641.
Wilson, D.S. & Hey, R.N., 1995. History of rift propagation and magnetization intensity for the Cocos-Nazca spreading center, *J. geophys. Res.,* **100**(B6), 10 041–10 056.
Wilson, D.S., Teagle, D.A.H. & Acton, G., 2003. *Proc. ODP, Init. Repts.,* eds ,Wilson, D., ,Teagle, D.A.H. & ,Acton, G., 1–117, **206,** College Station, TX (Ocean Drilling Program), doi:10.2973/odp.proc.ir.206.101.2003.
Winslow, D.M. & Fisher, A.T., 2015. Sustainability and dynamics of outcrop-to-outcrop hydrothermal circulation, *Nat. Commun.,* **6,** 7567, doi:10.1038/ncomms8567.
Winslow, D.M., Fisher, A.T., Stauffer, P.H., Gable, C.W. & Zyvoloski, G.A., 2016. Three-dimensional modeling of outcrop-to-outcrop hydrothermal circulation on the eastern flank of the Juan de Fuca Ridge, *J. geophys. Res.,* **121**(3), 1365–1382.
Worm, H.U., Böhm, V. & Bosum, W., 1996. 24. Implications for the sources of marine magnetic anomalies derived from magnetic logging in holes 504B AND 896A1, *Proc. Ocean Drill. Program, Sci. Results,* **148,** 331–338.

APPENDIX A: 1-D THERMAL CONDUCTION MODEL

To estimate the expected temperature at the SBI, we construct a 1-D steady-state-layered thermal conduction model consisting of a uniform layer of sediment overlying basaltic basement. We assume that thermal conductivity of each layer is constant, implying that

$$\frac{\mathrm{d}^2T}{\mathrm{d}z^2} = 0, \tag{A1}$$

where T is temperature and z is depth, subject to the conditions

$$\begin{aligned} &T_\mathrm{s}(z=0) = T_\mathrm{sw} \\ &\lambda_\mathrm{b}\frac{\mathrm{d}T_\mathrm{b}}{\mathrm{d}z}\bigg|_{z=h_\mathrm{b}} = q_\mathrm{b}. \end{aligned} \tag{A2}$$

Definitions and values of symbols are given in Table 2. Temperature and heat flux are continuous across the SBI. Consequently, in the sediment layer,

$$T_\mathrm{s}(z) = T_\mathrm{sw} + \frac{q_\mathrm{b}}{\lambda_\mathrm{s}}z; 0 \le z \le h_\mathrm{s} \tag{A3}$$

and the temperature at the SBI, relative to T_sw is

$$\Delta T_\mathrm{SBI}(h_\mathrm{s}) = \frac{q_\mathrm{b}h_\mathrm{s}}{\lambda_\mathrm{s}} \tag{A4}$$

Applying the half-space cooling model in eq. (1a) and assuming a constant sedimentation rate $h_\mathrm{s} = v_\mathrm{s}\tau$, we derive eq. (2).

APPENDIX B: THE WELL-MIXED AQUIFER MODEL

To estimate the lateral mass flow through the basement, we apply the well-mixed aquifer model of Langseth & Herman (1981; Fig. B1), where lateral advection dominates heat transport by conduction. The steady-state thermal balance is expressed as

$$\rho_\mathrm{f}c_\mathrm{f}uh_\mathrm{b}\frac{\mathrm{d}T(x)}{\mathrm{d}x} = q_\mathrm{b} - \lambda_\mathrm{s}\frac{T(x)}{h_\mathrm{s}}. \tag{B1}$$

The exponential solution to this equation by applying boundary conditions $T = T_0$ at $x = x_0$ yields (Kolandaivelu *et al.* 2017)

$$\frac{q\,(x)}{q_\mathrm{b}} = 1 + \left(\frac{q\,(x_0)}{q_\mathrm{b}} - 1\right)\left[\mathrm{e}^{\frac{a^*}{uh_\mathrm{b}h_\mathrm{s}}(x_0 - x)}\right]. \tag{B2}$$

For parameters shown in this appendix, refer to Table 2. Here $a* = \lambda_\mathrm{s}/\rho_\mathrm{f}c_\mathrm{f}$; $q(x)$ is heat flow at distance of x from x_0; $q(x_0)$ is the heat flow at distance x_0; x_0 is the distance of the first heat-flow measurement from the recharge outcrop (Table 1). An exponential fit based on the observed data and equating it to exponential in eq. (B2) provides the volumetric flow rate per unit length perpendicular to the flow direction, uh_b for a sediment thickness, h_s. Extrapolating the exponential fit to the data to the presumed discharge location from first measurement, heat flow at discharge, q_d, can be estimated and writing

$$q_\mathrm{d} = \lambda_\mathrm{s}\frac{T_\mathrm{d}}{h_\mathrm{s}} \tag{B3}$$

yields T_d and therefore the ΔT_r as recharge is assumed to occur at 0 °C.

Darcy's law can be modified and expressed as,

$$uh_\mathrm{b} = \frac{\alpha g k \Delta T_\mathrm{r} h_\mathrm{b}(h_\mathrm{b} + h_\mathrm{s})}{\nu L} \tag{B4}$$

This expression enables estimating formation permeability, kh_b. Substituting the calculated values from eqs (B2) and (B3), we can arrive at permeabilities, k, for $h_\mathrm{b} = 150$ m and 550 m.

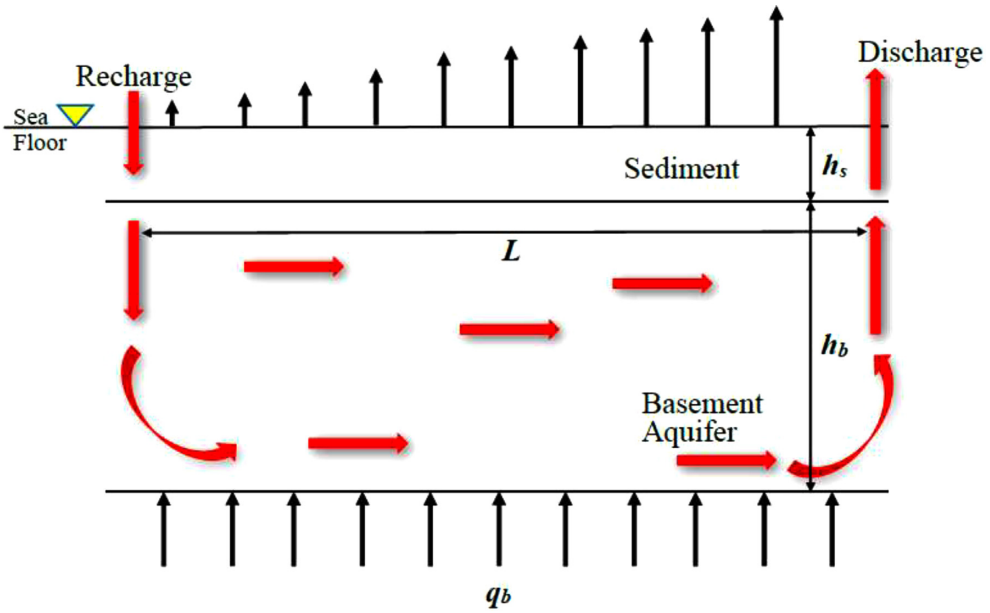

Figure B1. A well-mixed aquifer flow model modified from Langseth & Herman (1981). Refer to Table 2 for parameters shown in this figure.

APPENDIX C: HEAT FLOW NEAR A FAULT

To consider how conductive heat flow changes near a fault, we follow the approach outlined in Lowell (1975) in which the fault was modelled as vertical plane of height h and a constant temperature T_{sp}, placed at $x = 0$. Then assuming the seafloor is a horizontal plane $z = 0$, maintained at temperature $T = 0$, the steady-state temperature distribution in the rock adjacent to the fault can be found as outlined in Carslaw & Jaeger (1959). That is,

$$T(x,z) = \frac{T_{sp}}{\pi}\left[2\tan^{-1}\frac{z}{x} - \tan^{-1}\frac{z-h}{x} - \tan^{-1}\frac{z+h}{x}\right]. \quad \text{(C1)}$$

The conductive heat flux at the surface $z = 0$ is then

$$q = \frac{2T_{sp}\lambda_s}{\pi}\left[\frac{1}{x} - \frac{x}{x^2+h^2}\right]. \quad \text{(C2)}$$

If $x \ll h$, the second term in eq. (C2) may be neglected.